Computers and Structures 331 (2026) 108387

Contents lists available at ScienceDirect

Computers and Structures

journal homepage: www.elsevier.com/locate/cas

Topology optimization considering contact and stress constraints

Timo Schmidt, Mirko Keller*, Tom Klare, Robert Seifried

Institute of Mechanics and Ocean Engineering, Hamburg University of Technology, Eißendorfer Straße 42, 21073, Hamburg, Germany

ARTICLE INFO

Keywords:
Topology optimization
Stress constraints
Unilateral contact constraints
Node-to-segment contact
Segment-to-segment contact

ABSTRACT

This work advances stress-constrained topology optimization for frictionless unilateral contact problems involving large deformations and hyperelastic material behavior. The objective is to minimize the mass of a contact-constrained structure while enforcing stress constraints through local or global stress measures. Different contact coupling techniques based on Lagrange multipliers and penalty methods are investigated with respect to their applicability in stress-constrained optimization. The results show that stress-constrained optimization is considerably more sensitive to discretization errors at curved contact surfaces than common objectives such as compliance. Such errors may introduce artificial stresses that mislead the optimizer towards poorly performing designs. To address this issue, blending functions are used to retain the physical contact geometry during finite-element-based optimization, thereby avoiding the computational cost of very fine contact-surface discretizations. Furthermore, node-to-segment and segment-to-segment contact coupling are compared directly in stress-constrained topology optimization. The smoother contact-pressure and stress distributions provided by segment-to-segment coupling improve the optimization performance and lead to lighter feasible designs. Finally, local and global stress constraint formulations are compared, and an extension of the augmented Lagrangian approach is proposed to address convergence issues in challenging contact scenarios.

1. Introduction

Topology optimization is a powerful tool in computational engineering and structural design, and has been successfully applied to numerous academic benchmarks and real-world applications. However, there are still limitations since the optimized designs are calculated using computer-aided methods that rely on standard model assumptions, which may influence the performance of the optimized design. Therefore, it is crucial to guarantee that the model assumptions do not significantly affect the optimization. Two frequently neglected phenomena are stresses and unilateral contacts, as these are highly nonlinear local quantities that are difficult and expensive to take into account in the optimization. However, physically inaccurate modeling of these phenomena can result in optimized designs failing in real-world scenarios. In particular, the combination of unilateral contact constraints with stress constraints is rarely encountered in the context of topology optimization.

To the best of the authors' knowledge, only the following three publications [9,15,20] address this combination to some extent. Notably, none of these studies consider deformable contact surfaces modeled via node-to-segment or segment-to-segment contact formulations.

In fact, only Han et al. [20] consider the deformability of the contact surface. However, a node-to-node contact formulation is used, which can be applied if and only if the finite element discretizations of both contact partners are identical at the contact surface. This significantly limits the presented method.

Bruggi and Duysinx [9] introduce a stress-based approach that optimizes truss-like elastic structures considering unilateral behavior of material or unilateral rigid supports. Their approach minimizes compliance by initially considering only a limited set of unilateral constraints during the early iterations of the optimization. As their simulations reveal, after an initial phase, the optimization can proceed solely as a volume-constrained compliance minimization. This concept is of course not applicable to mass minimization.

The work of Fancello [15] is the closest to the presented work, as an actual mass minimization considering stress constraints and rigid contact boundary constraints is considered. In doing so, the rigid boundary constraints were imposed directly at the nodes of the contact surface and the stress constraints were imposed using a Lagrange Method. Although this methodology yields promising structural designs, Fancello reports significant difficulties in updating the Lagrange multipliers, leading to non-convergence issues. Additionally, the optimization of an L-shaped

* Corresponding author.
Email address: mirko.keller@tuhh.de (M. Keller).

https://doi.org/10.1016/j.compstruc.2026.108387
Received 3 February 2026; Accepted 19 July 2026
Available online 28 August 2026

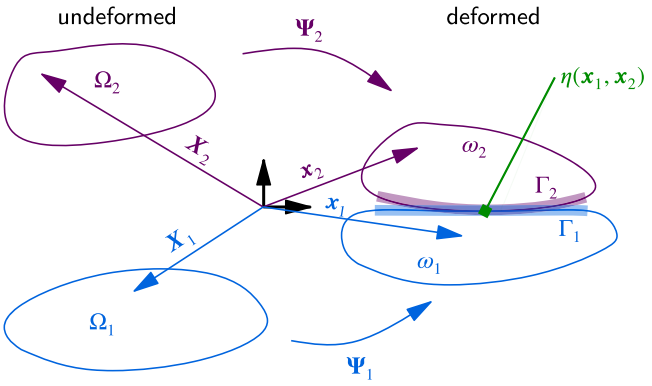

Fig. 1. Two hyperelastic bodies in contact with the contact surfaces Γ_1 and Γ_2 and the continuous contact gap function $\eta(\boldsymbol{x}_1, \boldsymbol{x}_2)$ along the contact surfaces.

design space incurred prohibitively high computational costs, which were deemed "unacceptable" by Fancello. More recently, works such as [13,37] modified the Lagrange Method significantly in order to overcome these convergence problems.

In the field of stress-constrained topology optimization mainly two methods dominate the field. In particular, these two are the so called local methods [13,37] using the an augmented Lagrangian method to impose the stress constraints and global methods based on aggregation functions [21,47]. A detailed overview of both methods can be found in [40]. Both methods will be used in this work to analyze which method is best suited for the application in contact-constrained topology optimization.

To our knowledge a framework for stress-constrained mass minimization that considers deformable contact surfaces has not yet been developed and is therefore proposed in this work. The focus is on frictionless contact, and both node-to-segment as well as segment-to-segment contact models are used. This work discusses the influence of these contact models on stress-constrained topology optimization. In addition, hyperelastic material behavior and large deformation are included in this presented framework.

It will be demonstrated that precisely modeling the contact surfaces' geometry is essential, as otherwise the stress-constrained optimization will be misled and poorly optimized designs will be observed. Therefore, achieving optimized designs that are independent of the discretization of the contact surfaces can only be expected if the contact geometry is represented with high accuracy. Additionally, the augmented Lagrangian method appears to be better suited for capturing local physical phenomena like contact, as it aligns more naturally with the underlying mechanics involved. Furthermore, an extended augmented Lagrangian method is proposed to avoid infeasible local minima in which optimizations based on the standard augmented Lagrangian formulation may become trapped. The extension increases the influence of stress constraints associated with elements in the vicinity of the contact surfaces, thereby improving the ability of the optimizer to obtain feasible designs in contact-dominated problems. Although the results presented in this work are demonstrated on 2D benchmark problems, the proposed methodology is not restricted to these assumptions and extends naturally to 3D domains.

The presented work is structured as follows. The Section 2 introduces the different contact models, while the Section 3 addresses the stress-constrained mass minimization problem. In Section 4 the influence of different contact models on the stress computation inside the design domain is discussed. Finally, Section 5 presents numerical results for two benchmark examples.

2. Contact mechanics

This section is intended to give a brief overview of contact mechanics and follows the structure of Wriggers [52], as several contact methods will be applied to benchmark problems in topology optimization. For a thorough literature review on contact-constrained topology optimization, the reader is referred to the work of Fernández et al. [16]. Detailed derivations and the treatment of special cases are discussed in the references given in each section.

In the first Section 2.1, the underlying total potential of the contact problem is introduced, to derive the equilibrium equation based on hyperelasticity in the following sections. In Section 2.2, the used contact constraint formulations are discussed, i.e. the Hertz-Signorini-Moreau contact condition and the unilateral penalty method. Next, the numerical coupling of the contact surfaces is discussed in Section 2.3. More precisely, the Section 2.3.1 deals with node-to-segment coupling while Section 2.3.2 introduces the mortar method, which is based on segment-to-segment coupling. The Section 2.4 introduces blending functions to accurately model curved surfaces in the finite element analysis. Finally, the nonlinear contact problem is formulated in Section 2.5.

2.1. Total potential of the contact problem

In this paper, a contact problem as shown in Fig. 1 is considered and hyperelastic material behavior is assumed. Thus, the principle of minimum potential energy [56] can be applied, as the existence of a strain energy function W is guaranteed. In doing so, the deformation state $\boldsymbol{\Psi}$ that minimizes the potential, is the solution of the equilibrium equations. The potential reads

$$\Pi_\Omega(\boldsymbol{\Psi}) = \int_\Omega W \,\mathrm{d}V - \int_{\Gamma_t} \boldsymbol{t}^* \cdot \boldsymbol{\Psi} \,\mathrm{d}A. \tag{1}$$

In the following, the cauchy stress tensor $\boldsymbol{\sigma}$, the first Piola-Kirchhoff stress tensor $\boldsymbol{P}$, the deformation gradient $\boldsymbol{F}$, the right Cauchy–Green tensor $\boldsymbol{C} = \boldsymbol{F}^{\mathrm{T}}\boldsymbol{F}$ and the Jacobian $J = \det(\boldsymbol{F})$ are introduced. Furthermore, the complete pull back of the Cauchy stress tensor into the undeformed configuration is done by introducing the second Piola-Kirchhoff stress tensor

$$\boldsymbol{S} = \boldsymbol{F}^{-1}\boldsymbol{P} = J\boldsymbol{F}^{-1}\boldsymbol{\sigma}\boldsymbol{F}^{-\mathrm{T}}. \tag{2}$$

In the context of Topology Optimization, various hyperelastic material models have been considered by [26]. In this work, a compressible Neo-Hookean material is considered. Its strain-energy function is

$$W = \frac{\mu}{2}(I_1 - 3) - \mu \ln(J) + \frac{\lambda}{2}\ln^2(J), \tag{3}$$

where $I_1 = \mathrm{tr}(\boldsymbol{C})$, Lame's material parameters are

$$\mu = \frac{\nu E}{(1+\nu)(1-2\nu)} \quad \text{and} \quad \lambda = \frac{E}{2(1+\nu)} \tag{4}$$

and the second Piola-Kirchhoff stress tensor is

$$S_{kl} = \lambda \ln(J) C^{-1}_{kl} + \mu(\delta_{kl} - C^{-1}_{kl}). \tag{5}$$

Using the finite element discretization, the nodal displacement field $\boldsymbol{u}_j$ and the external forces $\boldsymbol{q}_j$ for each contact partner $j \in [1, n_{\mathrm{cp}}]$ are introduced, where n_{cp} denotes the total number of contact partners. In doing so, the deformation of each contact partner is given by the continuous deformation $\boldsymbol{\Psi}_j$. Further, the stress-free initial state of the structure, referred to as the reference configuration, is $\boldsymbol{X}_j$ and $\boldsymbol{x}_j$ describes the state of the structure after applying external loads, also known as deformed configuration. Thus, the deformed state is given by $\boldsymbol{x}_j = \boldsymbol{X}_j + \boldsymbol{u}_j$.

Additionally, for topology optimization the modified SIMP approach [6,38] is used to parameterize each i-th finite element by means of a normalized density $\varphi^i_j \in [0, 1]$, where the index i is bounded by the total number of elements of each contact partner n^j_{el}. In doing so, the stiffness

of the i-th finite element is then determined by the penalized Young's modulus

$$E_j^i = E_j^{\min} + (\varphi_j^i)^p (E_j^{\max} - E_j^{\min}) \quad \text{with } i \in [1, n_{\text{el}}^j]. \tag{6}$$

The penalization factor is set to $p = 3$ and the void has a stiffness of $E_j^{\min}$, whereas the Young's modulus of the solid material is $E_j^{\max}$. The normalized densities of all elements are stored in the vector $\boldsymbol{\varphi}_j$ forming the design variables of the later defined optimization problem.

Thus, the displacements $\boldsymbol{u}_1$ and $\boldsymbol{u}_2$ of the contact problem must minimize the total potential

$$\Pi = \sum_j \left(\Pi_{\Omega_j} \right) + \Pi_{\text{C}}, \tag{7}$$

where Π_{C} is the potential arising from the contact constraints, which is discussed in the next section.

Further, the finite element discretization and the modified SIMP approach are used to derive the later needed residual of the potential from Eq. (1). It reads

$$\boldsymbol{r}_{\Omega_j}(\boldsymbol{\varphi}_j, \boldsymbol{u}_j) = \frac{\partial \Pi_{\Omega_j}}{\partial \boldsymbol{u}_j}. \tag{8}$$

2.2. Contact constraint formulation

The overall contact concept is visualized in Fig. 1. Here, the bodies 1 and 2 are in contact with each other at the contact surfaces Γ_1 and Γ_2. Consequently, the normal gap at any point of the contact surfaces is $\eta(\boldsymbol{x}_1, \boldsymbol{x}_2)$, where the coordinates $\boldsymbol{x}_1$ and $\boldsymbol{x}_2$ describe the corresponding closest points from one to the other contact surface $\Gamma_{1/2}$ in the deformed configuration. To prevent the contacting bodies from penetrating each other, a potential contact pressure ξ acting on the surfaces $\Gamma_{1/2}$ is introduced. In this work, the contact surfaces $\Gamma_{1/2}$ are approximately equal, so that the contact surface is $\Gamma_{\text{C}} \approx \Gamma_1 \approx \Gamma_2$. This is a common assumption in contact mechanics, since the parts of the two contact surfaces that are actually in contact are geometrically identical, apart from discretization errors. Deviations from the approximation $\Gamma_{\text{C}} \approx \Gamma_1 \approx \Gamma_2$ occur only in regions where the contact constraints are inactive, i.e. where no contact takes place. Consequently, the contact integrals can be evaluated only on one of the two contact surfaces. For the contact-coupling techniques introduced in the following, the integration is performed over the secondary contact surface and the resulting contact pressures are then mapped onto the primary contact surface. In order to compute the contact pressure, different contact conditions can be used. These conditions are introduced in a general form in this section, as the actual implementation depends on the used node-to-segment (Section 2.3.1) or segment-to-segment (Section 2.3.2) contact coupling.

2.2.1. Lagrange methods

In the finite element method, Lagrange methods are commonly used to enforce constraints by introducing additional unknowns, so-called Lagrange multipliers. In the context of contact mechanics, the Lagrange multipliers correspond physically to the contact pressure acting on the contact surfaces. This approach ensures that the contact constraints are precisely satisfied.

Hertz-Signorini-Moreau condition (HSM)

The so-called *Hertz-Signorini-Moreau* condition [30,39,52] for frictionless contact imposes that a gap η and contact pressure ξ cannot occur simultaneously, which is guaranteed if the following conditions are satisfied:

$$\xi \geq 0, \quad \eta(\boldsymbol{x}_1, \boldsymbol{x}_2) \geq 0, \quad \xi\, \eta(\boldsymbol{x}_1, \boldsymbol{x}_2) = 0. \tag{9}$$

Consequently, the following non-smooth function must hold over the whole contact surface

$$\Phi^{\text{HSM}} = -\xi + \max(0, \xi - \eta) = 0. \tag{10}$$

In practice, these conditions are imposed using a Lagrange multiplier method. The resulting potential is

$$\Pi_{\text{C}}^{\text{HSM}} = \int_{\Gamma_{\text{C}}} \xi\, \eta(\boldsymbol{x}_1, \boldsymbol{x}_2) \mathrm{d}A. \tag{11}$$

If the augmented Lagrange method is used, the potential is the sum of the potentials obtained by the Lagrange method Eq. (11) and the unilateral penalty method Eq. (14). The Lagrange method and the augmented Lagrange methods have been successfully applied in contact-constrained topology optimization; see e.g. [16,36,42,43].

2.2.2. Unilateral penalty method (UP)

Penalty Methods are the most commonly used contact constraint formulations [52]. Here, the contact conditions stated in Eq. (9) are weakened, so that small penetrations are admissible. The penetration is

$$\bar{\eta}(\boldsymbol{x}_1, \boldsymbol{x}_2) = \begin{cases} 0 & \text{, if } \eta(\boldsymbol{x}_1, \boldsymbol{x}_2) \geq 0 \\ -\eta(\boldsymbol{x}_1, \boldsymbol{x}_2) & \text{, else} \end{cases} \tag{12}$$

In doing so, the contact pressure ξ_{UP} is a function of the penetration

$$\xi_{\text{UP}} = \begin{cases} 0 & \text{, if } \bar{\eta}(\boldsymbol{x}_1, \boldsymbol{x}_2) \leq 0 \\ \epsilon_{\text{N}} \bar{\eta}(\boldsymbol{x}_1, \boldsymbol{x}_2) & \text{, else} \end{cases} \tag{13}$$

where $\epsilon_{\text{N}} > 0$ is the so-called penalty factor. The resulting contact potential is

$$\Pi_{\text{C}}^{\text{UP}} = \frac{1}{2} \int_{\Gamma_{\text{C}}} \epsilon_{\text{N}} \bar{\eta}(\boldsymbol{x}_1, \boldsymbol{x}_2)^2 \mathrm{d}A. \tag{14}$$

Here, no additional Lagrange multipliers are needed to compute the contact forces. In addition to the presented linear penalty method, a variety of nonlinear penalty methods have been developed to solve contact problems [52]. This group of methods has been successfully applied in contact-constrained topology optimization in e.g. [1,15,16,20,28,29].

2.3. Coupling techniques of the contact surfaces

While the previous section discussed contact characteristics for continuous domains, this section will focus on solving contact problems for discrete domains. In general, there are three concepts for coupling two finite element domains.

The most straightforward concept is the node-to-node method. Han et al. [20] used a node-to-node contact coupling in topology optimization framework successfully. However, this method has the major drawback that the discretizations of the contact surfaces of both bodies must be identical. This cannot be guaranteed in general, which strongly limits the method, especially when considering real-world applications. Therefore, this concept is not used in this work.

The node-to-segment contact coupling is a generalization of node-to-node coupling that considers both matching and non-matching discretizations at the contact surface. This technique is widely used in both research and commercial software. This coupling technique is discussed in Section 2.3.1.

The Section 2.3.2 introduces the segment-to-segment mortar method. Unlike the other two coupling techniques, the mortar method is based on a weak formulation of the contact constraint formulation.

2.3.1. Node-to-segment contact (n2s)

The node-to-segment (n2s) algorithm was first introduced to solve purely geometric non-penetration conditions [19,23,24] and was later further developed by [5,18,31,41,50–52].

The node-to-segment algorithm is based on a *Primary-Secondary relation*[1] and its main concept is visualized in Fig. 2. In doing so, the contact

[1] also known as master-slave relation in the literature.

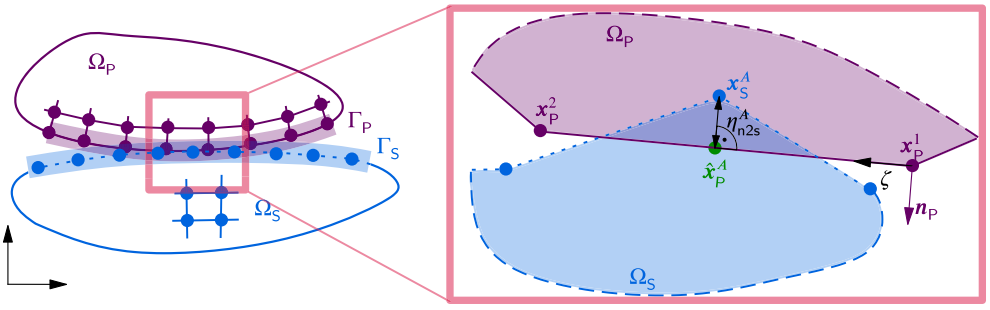

Fig. 2. Node-to-segment contact for the A-th secondary contact node x_S^A and the corresponding primary segment of Γ_P.

surface Γ_P of the primary body Ω_P is considered as finite segments, while the contact surface Γ_S of the secondary body Ω_S is only represented by its nodes obtained from the finite element discretization. As the contact normal direction must be perpendicular to the contact surface, the contact normal direction of the primary body n_P is chosen. Therefore, the outward normal of each finite segment located at the primary contact surface must be computed and is used to determine the normal gap η^A between each secondary node and the corresponding primary segment. Due to this, there exist special cases where the projection of the secondary node onto the discrete primary contact surface fails or is not unique. These cases are also known as *out-of-both* and *in-of-both*. In this work, both cases are treated using the method based on the rotation of the normal vector, see [53]. A more detailed review of the handling of the special cases can be found in [53]. Furthermore, it is worth mentioning that only the nodes of the secondary contact surface will satisfy the contact constraints, while the nodes of the primary contact surface can violate the contact constraints, i.e. nodes of the primary surface can penetrate the secondary body.

Finally, it should be noted that the presented classic node-to-segment algorithm does not pass the *Patch-Test* [46]. This test is designed to investigate whether a contact algorithm accurately transmits a constant normal stress. Algorithms that fail the patch test introduce solution errors that do not necessarily decrease with mesh refinement. Node-to-segment formulations addressing this problem are presented in e.g. [10,54].

Concept of node-to-segment

In Fig. 2, the utilized node-to-segment algorithm is shown for the A-th contact node x_S^A of the secondary contact surface Γ_S. In doing so, each node of Γ_S is mapped onto the corresponding finite segment of the primary contact surface Γ_P. In 2D, the primary segment consists of the nodes x_P^1 and x_P^2 and the projection point on the primary segment is $\hat{x}_P^A$. Furthermore, the mapping is performed based on the primary normal direction n_P. Consequently, the local coordinates $\hat{\zeta}_P$ of the projection point inside the primary segment must be computed.

Until now, all coordinates $x_{P/S}$ are represented in the deformed configuration. However, any discrete point p of the deformed configuration is given by

$$x_{P/S}^p = X_{P/S}^p + u_{P/S}^p, \tag{15}$$

where $X_{P/S}^p$ is the position of the point p in the reference configuration, while $u_{P/S}^p$ is the nodal displacement of point p.

Note that, the normal direction n_P is a function of the displacements of the primary contact surface. Thus, the local coordinates of the projection point $\hat{\zeta}_P$ have to be recomputed for the current displacements of the primary contact surface. The projection point is

$$\hat{x}_P^A = \sum_{k=1}^{m} M^k(\hat{\zeta}_P)(X_P^k + u_P^k), \tag{16}$$

where m is the number of shape functions of the primary segment and M^k are the shape functions of the finite segment of the primary contact surface. In consequence, the gap function of the A-th secondary contact node is

$$\eta_{n2s}^A = (x_S^A - \hat{x}_P^A) \cdot n_P = \left(x_S^A - \sum_{k=1}^{m} M^k(\hat{\zeta}_P)(X_P^k + u_P^k)\right) \cdot n_P. \tag{17}$$

Lagrange contact constraint

If the Lagrange method is used, the contact potential from Eq. (11) is approximated by the sum over all contact nodes of the secondary contact surface Γ_S as

$$\Pi_C^{HSM} \approx \Pi_{C,n2s}^{HSM} = \sum_A \xi^A \eta_{n2s}^A, \tag{18}$$

where ξ^A is the nodal contact force acting at the A-th node of Γ_S. Further, the non-smooth contact function of Eq. (10) must be satisfied by the A-th node of Γ_S. It reads

$$\Phi_{n2s}^{HSM} = -\xi^A + \max(0, \xi^A - \eta_{n2s}^A) = 0. \tag{19}$$

Consequentially, the residual r of the contact problem is derived from Eqs. (7) and (18). It reads

$$r_{n2s}^{LM}(\varphi, \begin{bmatrix} u_S \\ u_P \\ P_N \end{bmatrix}) = \begin{Bmatrix} \begin{bmatrix} r_{\Omega_S}(\varphi_S, u_S) \\ r_{\Omega_P}(\varphi_P, u_P) \end{bmatrix} + \begin{bmatrix} C_{S,n2s} \\ C_{P,n2s} \end{bmatrix}^T P_N \\ \Phi_{n2s}^{HSM} \end{Bmatrix} \tag{20}$$

where the vector P_N holds all nodal contact forces ξ^A of Γ_S and Φ_{n2s}^{HSM} holds all contact functions from Eq. (19). The mapping matrices of the nodal contact forces P_N are defined as

$$C_{S,n2s} = \frac{\partial \eta_{n2s}(u_S, u_P)}{\partial u_S}, \quad C_{P,n2s} = \frac{\partial \eta_{n2s}(u_S, u_P)}{\partial u_P}. \tag{21}$$

Here, $\eta_{n2s}(u_S, u_P)$ is a vector holding all nodal gaps of Γ_S, see Eq. (17).

Unilateral penalty contact constraint

If the unilateral penalty method is used as a contact constraint, the penetration in Eq. (12) must be adopted for the node-to-segment method. The penetration of the A-th contact node of Γ_S is obtained by inserting Eq. (17) into Eq. (12). It reads

$$\bar{\eta}_{n2s}^A = \begin{cases} 0 & , \text{if} \eta_{n2s}^A \geq 0 \\ -\eta_{n2s}^A & , \text{else} \end{cases} \tag{22}$$

The contact potential from Eq. (14) is approximated by the following sum over the contact nodes of Γ_S

$$\Pi_C^{UP} \approx \Pi_{C,n2s}^{UP} = \frac{1}{2} \sum_A \epsilon_N \left(\bar{\eta}_{n2s}^A\right)^2. \tag{23}$$

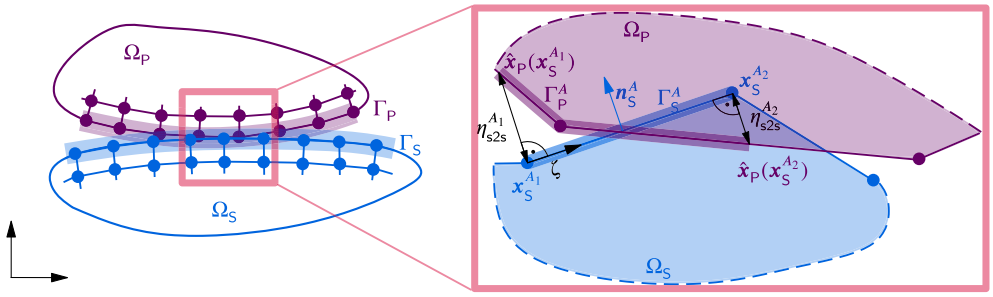

Fig. 3. Segment-to-segment contact for the A-th secondary contact segment Γ_S^A and its projection Γ_P^A onto the primary segments of Γ_P.

The residual $\boldsymbol{r}$ of the contact problem is derived from the Eq. (7) and Eq. (23). It reads

$$\boldsymbol{r}_{n2s}^{UP}(\boldsymbol{\varphi}, \begin{bmatrix}\boldsymbol{u}_S \\ \boldsymbol{u}_P\end{bmatrix}) = \begin{bmatrix}\boldsymbol{r}_{\Omega_S}(\boldsymbol{\varphi}_S, \boldsymbol{u}_S) \\ \boldsymbol{r}_{\Omega_P}(\boldsymbol{\varphi}_P, \boldsymbol{u}_P)\end{bmatrix} + \epsilon_N \begin{bmatrix}\bar{\boldsymbol{C}}_{S,n2s} \\ \bar{\boldsymbol{C}}_{P,n2s}\end{bmatrix}^T \bar{\boldsymbol{\eta}}_{n2s}(\boldsymbol{u}_S, \boldsymbol{u}_P) \tag{24}$$

where the mapping matrices are defined as

$$\bar{\boldsymbol{C}}_{S,n2s} = \frac{\partial \bar{\boldsymbol{\eta}}_{n2s}(\boldsymbol{u}_S, \boldsymbol{u}_P)}{\partial \boldsymbol{u}_S}, \quad \bar{\boldsymbol{C}}_{P,n2s} = \frac{\partial \bar{\boldsymbol{\eta}}_{n2s}(\boldsymbol{u}_S, \boldsymbol{u}_P)}{\partial \boldsymbol{u}_P}. \tag{25}$$

Here, $\bar{\boldsymbol{\eta}}_{n2s}(\boldsymbol{u}_S, \boldsymbol{u}_P)$ is a vector holding all nodal penetrations of Γ_S, as seen in Eq. (22).

2.3.2. Segment-to-segment contact (s2s) - the mortar method

In this section, a mortar segment-to-segment (s2s) method is discussed. Once again a *primary-secondary relation* is used. In contrast to the node-to-segment methods, both the primary and secondary contact surfaces are considered to be finite segments. The first formulations were developed by [41] and further extended for interface and contact problems, including friction and large deformations in two and three dimensions by, e.g. [32–34,49]. In addition, small and large deformation mortar methods have been successfully applied to topology optimization. Objectives such as maximizing the strain energy or total contact force and minimizing the compliance or total energy are considered [16,35,42], yet a stress-constrained mass minimization has not been considered.

The mortar method used in this work has been successfully applied in topology optimization by [42] and is based on [32,49].

Concept of the mortar method

The main idea of the segment-to-segment method is visualized in Fig. 3. Here, the whole discretized secondary contact boundary Γ_S is mapped onto the discretized primary contact boundary Γ_P. In doing so, the secondary contact boundary Γ_S is considered segment by segment.

In the magnification of Fig. 3, the highlighted contact surfaces show the projection of the A-th secondary segment Γ_S^A onto the segments of the primary contact surface Γ_P^A. Furthermore, the contact gaps $\eta_{s2s}^{A_{1/2}}$ at the secondary nodes $\boldsymbol{x}_S^{A_1}$ and $\boldsymbol{x}_S^{A_2}$ are shown in Fig. 3. The contact gap $\eta_{n2s}^{A_1}$ at $\boldsymbol{x}_S^{A_1}$ is larger than zero, while the contact gap $\eta_{n2s}^{A_2}$ is negative. Thus, the visualized segment is partially in contact.

As all segments of Γ_S and Γ_P are based on the chosen finite element discretization, all approximations made will be applied to the contact potential Eq. (11) or (14) respectively. Consequently, an actual weak formulation of the contact potential is derived which is based on all global shape functions living on one of the contact surfaces Γ_S and Γ_P, respectively.

As a result, the contact gap of the A-th segment η_{s2s}^A depends on the active shape functions of the contact surface. In doing so, $N_S^{A_i}$ represents the shape functions of the A-th secondary contact surface Γ_S^A, while $M_P^{A_j}$ are the shape functions of the projected primary contact surface Γ_P^A. Note that $M_P^{A_j}$ can include the shape functions of adjacent primary segments, as it is the projection of the secondary segment onto the primary contact surface. Within each secondary segment, the normal contact gap is defined as the difference between any point $\boldsymbol{x}_S^A$ of Γ_S^A and its projection point $\hat{\boldsymbol{x}}_P(\boldsymbol{x}_S^A)$ on Γ_P^A. The projected point $\hat{\boldsymbol{x}}_P(\boldsymbol{x}_S^A)$ of the primary surface is found using the normal direction $\boldsymbol{n}_S^A$ of the deformed secondary segment. The contact gap reads

$$\eta_{s2s}^A = (\hat{\boldsymbol{x}}_P(\boldsymbol{x}_S^A) - \boldsymbol{x}_S^A) \cdot \boldsymbol{n}_S^A. \tag{26}$$

Any point on the secondary contact surface $\boldsymbol{x}_S^A$ can be expressed using the shape functions of the segment $N_S^{A_i}$ and the segment nodes $\boldsymbol{x}_S^{A_i}$. Each secondary segment is approximated with n shape functions. With Eq. (15), any point on the secondary segment Γ_S^A is described by

$$\boldsymbol{x}_S^A = \sum_{i=1}^{n} N_S^{A_i} \boldsymbol{x}_S^{A_i} = \sum_{i=1}^{n} N_S^{A_i} (\boldsymbol{X}_S^{A_i} + \boldsymbol{u}_S^{A_i}). \tag{27}$$

Similarly, the projected point $\hat{\boldsymbol{x}}_P(\boldsymbol{x}_S^A)$ can be expressed using the shape functions $M_P^{A_j}$ of all the primary segments involved and its nodes $\boldsymbol{x}_P^{A_j}$. Thus, any point in the projected segment Γ_P^A is

$$\hat{\boldsymbol{x}}_P(\boldsymbol{x}_S^A) = \sum_{j=1}^{m} M_P^{A_j} \boldsymbol{x}_P^{A_j} = \sum_{j=1}^{m} M_P^{A_j} (\boldsymbol{X}_P^{A_j} + \boldsymbol{u}_P^{A_j}). \tag{28}$$

In Eq. (28), m is the number of active shape functions of the projection of the secondary segment onto the primary contact surface. In the illustrated projection of Fig. 3, the number of active shape functions is $m = 3$, however, it must be determined for each segment of Γ_S individually. Inserting Eqs. (27) and (28) into Eq. (26) leads to the segment-to-segment contact gap

$$\eta_{s2s}^A = \Big(\sum_{j=1}^{m} M_P^{A_j} (\boldsymbol{X}_P^{A_j} + \boldsymbol{u}_P^{A_j}) - \sum_{i=1}^{n} N_S^{A_i} (\boldsymbol{X}_S^{A_i} + \boldsymbol{u}_S^{A_i}) \Big) \cdot \boldsymbol{n}_S^A. \tag{29}$$

Rearranging and introducing the initial gap

$$g_{s2s}^A = \Big(\sum_{j=1}^{m} M_P^{A_j} \boldsymbol{X}_P^{A_j} - \sum_{i=1}^{n} N_S^{A_i} \boldsymbol{X}_S^{A_i} \Big) \cdot \boldsymbol{n}_S^A \tag{30}$$

results in a compact form of the segment-to-segment contact gap of the A-th secondary contact segment

$$\eta_{s2s}^A = g_{s2s}^A + \Big(\sum_{j=1}^{m} M_P^{A_j} \boldsymbol{u}_P^{A_j} - \sum_{i=1}^{n} N_S^{A_i} \boldsymbol{u}_S^{A_i} \Big) \cdot \boldsymbol{n}_S^A. \tag{31}$$

The finite element approximations of the contact pressure must also be considered, so that the contact force inside the A-th secondary segment is defined as

$$\lambda_{s2s}^A = \sum_{i=1}^{n} N_S^{A_i} \lambda_S^{A_i}, \tag{32}$$

where $\lambda_S^{A_i}$ is the nodal contact pressure of the A-th secondary segment. In the mortar method, the contact pressure is usually defined over the

secondary contact surface [33]. In order to compute the nodal contact forces vector $\boldsymbol{P}_{\mathrm{N}}$ acting at the nodes of Γ_{S}, the Eqs. (31) and (32) are used to calculate the weighted mortar nodal gaps

$$\boldsymbol{\eta}_{\mathrm{s2s}} = \bigboxplus_{A} \int_{\Gamma_{\mathrm{S}}^{A}} \sum_{i=1}^{n} N_{\mathrm{S}}^{A_i} \eta_{\mathrm{s2s}}^{A} \mathrm{d}A = \boldsymbol{C}_{\mathrm{S,s2s}} \boldsymbol{u}_{\mathrm{S}} + \boldsymbol{C}_{\mathrm{P,s2s}} \boldsymbol{u}_{\mathrm{P}} - \boldsymbol{g}, \tag{33}$$

where $\bigboxplus_{A}$ stands for a segment-by-segment assembly process along Γ_{S}. This process is similar to the assembly process of the stiffness matrix. Furthermore, the mapping matrices $\boldsymbol{C}_{\mathrm{S,s2s}}$ and $\boldsymbol{C}_{\mathrm{P,s2s}}$, as well as the nodal contact gaps $\boldsymbol{g}$ can be efficiently calculated in a manner similar. More precisely, the following segment-wise integrals must be solved

$$\boldsymbol{C}_{\mathrm{S,s2s}} = \bigboxplus_{A} \int_{\Gamma_{\mathrm{S}}^{A}} \sum_{i=1}^{n} \sum_{j=1}^{n} N_{\mathrm{S}}^{A_i} N_{\mathrm{S}}^{A_j} \boldsymbol{n}_{\mathrm{S}}^{A} \mathrm{d}A, \tag{34}$$

$$\boldsymbol{C}_{\mathrm{P,s2s}} = -\bigboxplus_{A} \int_{\Gamma_{\mathrm{S}}^{A}} \sum_{i=1}^{n} \sum_{j=1}^{m} N_{\mathrm{S}}^{A_i} M_{\mathrm{P}}^{A_j} \boldsymbol{n}_{\mathrm{S}}^{A} \mathrm{d}A, \tag{35}$$

$$\boldsymbol{g} = \bigboxplus_{A} \int_{\Gamma_{\mathrm{S}}^{A}} \sum_{i=1}^{n} N_{\mathrm{S}}^{A_i} g_{\mathrm{s2s}}^{A} \mathrm{d}A. \tag{36}$$

In Eq. (35), the integral to compute $\boldsymbol{C}_{\mathrm{P,s2s}}$ is the so-called mortar integral that must be solved with a higher order quadrature rule. In this work, the Lobatto rule with 10 integration points is used as it was already successfully applied in the context of topology optimization by [42].

Lagrange contact constraint

In contrast to the node-to-segment coupling, the contact potential of Eq. (11) is not approximated by a sum over the nodes of the secondary contact surface Γ_{S}. Instead, the integral over Γ_{S} is subdivided into a sum of segment-wise integrals of the contact boundary Γ_{S}^{A} which are integrated using finite element approximations. Thus, the potential of the Lagrange method Eq. (11) is approximated using Eqs. (31) and (32). The potential reads

$$\Pi_{\mathrm{C}}^{\mathrm{HSM}} \approx \Pi_{\mathrm{C,s2s}}^{\mathrm{HSM}} = \sum_{A} \int_{\Gamma_{\mathrm{S}}^{A}} \lambda_{\mathrm{s2s}}^{A} \eta_{\mathrm{s2s}}^{A} \mathrm{d}A. \tag{37}$$

The residual $\boldsymbol{r}$ can then be derived by inserting Eq. (37) into the total potential Eq. (7) and taking the derivative with respect to the nodal displacements $\boldsymbol{u}_{\mathrm{S}}$ and $\boldsymbol{u}_{\mathrm{P}}$ and the nodal contact force vector $\boldsymbol{P}_{\mathrm{N}}$. The residual reads

$$\boldsymbol{r}_{\mathrm{s2s}}^{\mathrm{LM}}(\boldsymbol{\varphi}, \begin{bmatrix} \boldsymbol{u}_{\mathrm{S}} \\ \boldsymbol{u}_{\mathrm{P}} \\ \boldsymbol{P}_{\mathrm{N}} \end{bmatrix}) = \begin{Bmatrix} \begin{bmatrix} \boldsymbol{r}_{\Omega_{\mathrm{S}}}(\boldsymbol{\varphi}_{\mathrm{S}}, \boldsymbol{u}_{\mathrm{S}}) \\ \boldsymbol{r}_{\Omega_{\mathrm{P}}}(\boldsymbol{\varphi}_{\mathrm{P}}, \boldsymbol{u}_{\mathrm{P}}) \end{bmatrix} + \begin{bmatrix} \boldsymbol{C}_{\mathrm{S,s2s}} \\ \boldsymbol{C}_{\mathrm{P,s2s}} \end{bmatrix}^{\mathrm{T}} \boldsymbol{P}_{\mathrm{N}} \\ \boldsymbol{\Phi}_{\mathrm{s2s}}^{\mathrm{HSM}} \end{Bmatrix} \tag{38}$$

where the mapping matrices $\boldsymbol{C}_{\mathrm{S,s2s}}$ and $\boldsymbol{C}_{\mathrm{P,s2s}}$ are identical to Eqs. (34) and (35), respectively.

Finally, the contact function of Eq. (10) must be adapted for the segment-to-segment approach. This is straightforward as the contact function can be applied directly to each nodal contact force ξ^k and its corresponding nodal gap η_{s2s}^{k}. Here, the index k represents the k-th entry of the nodal contact force vector $\boldsymbol{P}_{\mathrm{N}}$ and the weighted mortar nodal gaps $\boldsymbol{\eta}_{\mathrm{s2s}}$, respectively. The resulting contact function reads

$$\Phi_{\mathrm{s2s}}^{\mathrm{HSM}} = -\xi^k + \max(0, \xi^k - \eta_{\mathrm{s2s}}^{k}) = 0. \tag{39}$$

Unilateral penalty contact constraint

The potential of the unilateral penalty method (UP) is based on the chosen finite element approximations. In this work, the weighted mortar nodal gap vector introduced in Eq. (33) is used, which must be transformed for each secondary contact node into weighted mortar nodal penetrations:

$$\bar{\eta}_{\mathrm{s2s}}^{k} = \begin{cases} 0 & , \text{if } \eta_{\mathrm{s2s}}^{k} \geq 0 \\ -\eta_{\mathrm{s2s}}^{k} & , \text{else} \end{cases} \tag{40}$$

Thus, the contact potential of Eq. (14) is approximated by a sum over all contact nodes of the secondary contact surface

$$\Pi_{\mathrm{C}}^{\mathrm{UP}} \approx \Pi_{\mathrm{C,s2s}}^{\mathrm{UP}} = \frac{1}{2} \sum_{k} \epsilon_{\mathrm{N}} \bar{\eta}_{\mathrm{s2s}}^{k} \bar{\eta}_{\mathrm{s2s}}^{k}, \tag{41}$$

where each penetration $\bar{\eta}_{\mathrm{s2s}}^{k}$ is obtained based on the mortar method presented.

In doing so, the contact residual using the unilateral penalty method in combination with the segment-to-segment approach is given by

$$\boldsymbol{r}_{\mathrm{s2s}}^{\mathrm{UP}}(\boldsymbol{\varphi}, \begin{bmatrix} \boldsymbol{u}_{\mathrm{S}} \\ \boldsymbol{u}_{\mathrm{P}} \end{bmatrix}) = \begin{bmatrix} \boldsymbol{r}_{\Omega_{\mathrm{S}}}(\boldsymbol{\varphi}_{\mathrm{S}}, \boldsymbol{u}_{\mathrm{S}}) \\ \boldsymbol{r}_{\Omega_{\mathrm{P}}}(\boldsymbol{\varphi}_{\mathrm{P}}, \boldsymbol{u}_{\mathrm{P}}) \end{bmatrix} + \epsilon_{\mathrm{N}} \begin{bmatrix} \bar{\boldsymbol{C}}_{\mathrm{S,s2s}} \\ \bar{\boldsymbol{C}}_{\mathrm{P,s2s}} \end{bmatrix}^{\mathrm{T}} \bar{\boldsymbol{\eta}}_{\mathrm{s2s}}(\boldsymbol{u}_{\mathrm{S}}, \boldsymbol{u}_{\mathrm{P}}) \tag{42}$$

The mapping matrices $\bar{\boldsymbol{C}}_{\mathrm{S,s2s}}$ and $\bar{\boldsymbol{C}}_{\mathrm{P,s2s}}$ are defined based on Eqs. (34) and (35) as follows

$$\bar{\boldsymbol{C}}_{\mathrm{S,s2s}} = -\boldsymbol{C}_{\mathrm{S,s2s}} \text{ and } \bar{\boldsymbol{C}}_{\mathrm{P,s2s}} = -\boldsymbol{C}_{\mathrm{P,s2s}}. \tag{43}$$

2.4. Blending of the contact geometry

In numerical applications, the quality of the computed contact pressure depends heavily on the quality of the finite element (FE) discretization used. This can be a major challenge because in topology optimization, the contact problem must be solved in each optimization iteration. In order to circumvent the additional numerical cost that comes with significantly finer FE discretizations along the contact surfaces, blending functions are proposed in this work; see [17,57].

The concept of blending is further visualized in Fig. 4(a). Although blending functions are not limited to 2D, the following explanation focuses on a quadrilateral element whose edge E_1 is part of a curved surface. In principle, all edges and faces could be blended separately. However, this is not required for the present work and is therefore not considered. For further details on blending functions, the reader is referred to [17,57].

The actual geometry of the curved surface is parameterized by the function $\boldsymbol{E}_b = [E_{\mathrm{x}}(\zeta_1), E_{\mathrm{y}}(\zeta_1)]$, where $\boldsymbol{\zeta} \in [0, 1]$ denotes the local coordinates. The corresponding bilinear mapping is augmented by blending the difference between the curved edge $\boldsymbol{E}_1$ and the straight line connecting the nodes N_1 and N_2 into the element interior. The resulting augmented mapping reads

$$\boldsymbol{x} = \sum_{i=1}^{4} N_{1,1}^{N_i}(\boldsymbol{\zeta}) \boldsymbol{X}_i + \frac{1-\zeta_2}{2} \left(\boldsymbol{E}_b(\zeta_1) - \left(\frac{1-\zeta_1}{2} \boldsymbol{X}_1 + \frac{1+\zeta_1}{2} \boldsymbol{X}_2 \right) \right), \tag{44}$$

where, by construction, the opposite edge E_3 remains unaffected by the blended surface correction.

As shown in Fig. 4, blending functions provide a general method for accurately modeling the geometry of a surface without introducing discretization errors. Fig. 4(b) visualizes a standard FE discretization along a curved contact surface (red dotted). Artificial gaps as well as penetrations along the discrete contact surfaces of both domains are observed. These numerical artifacts result in inaccurate contact pressures that in turn will result in artificial stress peaks in the vicinity of the contact surfaces. As demonstrated later in this work, these artificial stress peaks dominate the stress-constrained optimization, so that the optimized designs cannot be used in practice. In contrast, Fig. 4(c)

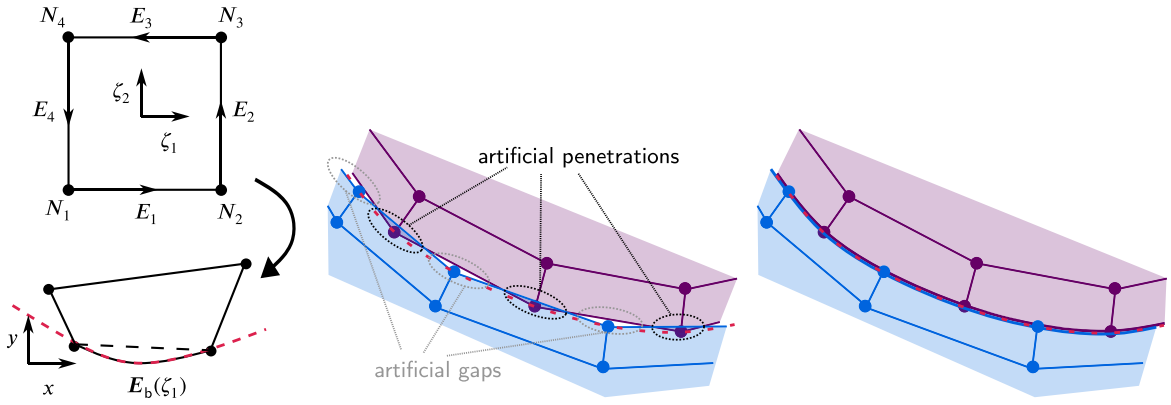

(a) Concept of blending. (b) Standard FE discretization. (c) Blended FE discretization.

Fig. 4. FE discretizations with and without blended segments along the exact geometry of the contact surface (red dotted).

visualizes the blended discretization, where each finite element located at the contact support has a curved surface so that contact constraints can be evaluated at any point of the contact surface without introducing artificial gaps or penetrations. In doing so, accurate contact pressures can be guaranteed. To the best of the authors' knowledge, this problem is not addressed in contact-constrained topology optimization literature, as this phenomenon is only present at curved contact surfaces. In addition, standard objectives such as the compliance are less sensitive to inaccurate contact pressures. However, when performing stress-constrained optimization along curved contact surfaces, one must guarantee accurate contact pressures for any design during the optimization process, as any optimization will be misled otherwise.

2.5. Solving the contact problem

The residual $\boldsymbol{r}$ of the node-to-segment coupling technique, see Eq. (20) or Eq. (24), as well as the residual of the segment-to-segment coupling technique, see Eq. (38) or Eq. (42), have now been defined for the nonlinear and non-smooth contact problem. In this work, the standard Newton method with numerical damping of the PETSc library is used [2–4]. In rare cases, where the Newton method fails to converge, a bisection line search is employed to provide a robust backup solution. To treat the discontinuity of the contact problem, the Jacobian of the nonlinear problem is evaluated for the current state. Thus, the search direction of the nonlinear solver only considers the current active set of contact constraints depending on the current state as similarly done in [15,16,35,42,43].

Even though a discontinuous contact problem is considered, the line search is applied successfully. In order to update the state vector $\boldsymbol{x}$ of the nonlinear problem, the Jacobian matrix must be computed. If the Lagrange method is used, the state vector is $\boldsymbol{x}^{\mathrm{LM}} = (\boldsymbol{u}_{\mathrm{S}}, \boldsymbol{u}_{\mathrm{P}}, \boldsymbol{P}_{\mathrm{N}})^{\mathrm{T}}$. For the unilateral penalty method the state vector is $\boldsymbol{x}^{\mathrm{UP}} = (\boldsymbol{u}_{\mathrm{S}}, \boldsymbol{u}_{\mathrm{P}})^{\mathrm{T}}$. The Jacobian

$$\boldsymbol{J}_{\mathrm{c}}(\boldsymbol{\varphi}, \boldsymbol{x}) = \frac{\partial \boldsymbol{r}_{\mathrm{c}}(\boldsymbol{\varphi}, \boldsymbol{x})}{\partial \boldsymbol{x}} \tag{45}$$

is obtained based on the linearization of the corresponding residual $\boldsymbol{r}_{\mathrm{c}}(\boldsymbol{\varphi}, \boldsymbol{x})$. Thus, the linearization of the residuals must be derived for each of the four contact concepts separately; see Eq. (20), Eq. (24), Eq. (38) and Eq. (42).

Given a density distribution $\tilde{\boldsymbol{\varphi}}$ and a guess for the state vector $\tilde{\boldsymbol{x}}$, the search direction of the line-search algorithm is

$$\boldsymbol{s} = \left(\boldsymbol{J}_{\mathrm{c}}(\tilde{\boldsymbol{x}}, \tilde{\boldsymbol{\varphi}})\right)^{-1} \boldsymbol{r}_{\mathrm{c}}(\tilde{\boldsymbol{x}}, \tilde{\boldsymbol{\varphi}}). \tag{46}$$

3. Optimization with stress constraints

In this work, the objective is to minimize the mass while satisfying the stress constraint in any finite element. In doing so, the introduced contact problem must be solved, where any residual of the contact models and contact coupling techniques can be considered. In order to increase readability, the residual of the contact problem derived in Section 2.5 is denoted by $\boldsymbol{r}_{\mathrm{c}}(\boldsymbol{\varphi}, \boldsymbol{x})$. Note that the presented mass minimization problem is similar for node-to-segment as well as segment-to-segment contact coupling techniques. The mass minimization problem is stated as

$$\begin{aligned} &\min_{\boldsymbol{\varphi}} m(\boldsymbol{\varphi}) = \frac{1}{v_{\mathrm{t}}} \sum_{i=1}^{n_{\mathrm{el}}} v_i \varphi_i \\ &\text{s.t.} \begin{cases} g_j \leq 0, \quad \forall\, j = 1, \dots, n_{\mathrm{el}} \\ \boldsymbol{r}_{\mathrm{c}}(\boldsymbol{\varphi}, \boldsymbol{x}) = \boldsymbol{0} \\ \boldsymbol{0} \leq \boldsymbol{\varphi} \leq \boldsymbol{1} \end{cases} \end{aligned} \tag{47}$$

where v_i is the volume of the i-th finite element and g_j is the stress constraint of the j-th finite element. In Eq. (47), the actual mass of the current design is normalized by the total volume v_{t} of the design space.

In the following sections, the main challenges in stress-constrained topology optimization are discussed. The first Section 3.1 discusses the interpretation of grayscale elements during optimization. In Section 3.2, the so-called singular optima phenomenon is discussed and the concept of vanishing constraints is introduced to overcome this challenge. Furthermore, solving the optimization problem of Eq. (47) is inefficient due to the high number of constraints, since a stress limit is imposed on each finite element separately. This is impractical, which is why a more efficient local or a global stress constraint strategy must be used so that gradient-based topology optimization can be efficiently applied. Therefore, Section 3.3 deals with a local strategy using the augmented Lagrangian method for stress constraints, while Section 3.4 follows a global strategy using an aggregation function. The design update is performed using the Method of Moving Asymptotes [44], so a sensitivity analysis must be performed. Details on the sensitivity analysis can be found in the Appendix A.

Note that the Lagrange method enforcing the contact constraints must not be confused with the following augmented Lagrangian method to enforce the stress constraints of Section 3.3. More precisely, a Lagrange method can be used to fulfill the contact constraints, while a second augmented Lagrangian method can be employed to solve the stress-constrained topology optimization problem. In order to prevent confusion, the phrase "Lagrange method" is used only in the context

of contact constraints, while the phrase "augmented Lagrangian approach" is used for the augmented Lagrangian method addressing the stress-constrained optimization.

3.1. Stress computation

In density-based topology optimization, the normalized densities of each finite element $\boldsymbol{\varphi} \in [\mathbf{0}, \mathbf{1}]$ are the design variables, so that non-binary or so-called grayscale densities occur during the optimization process. This is unavoidable, as the SIMP approach is used, and a suitable stress criterion must take this into account. Non-binary element densities can physically be interpreted as porous elements with an unidentified microstructure [6]. Consequently, a stress criterion must be applicable to solid and porous elements, as well as void elements. For the latter, the stress should obviously vanish as the normalized density $\varphi \to 0$.

This is in some sense similar to homogenization of the stiffness of porous elements, where the SIMP homogenization has proven to be effective. However, homogenized stress measures in general lack physical meaning, and the use of a SIMP homogenized stress criterion leads either to artificial removal of material during optimization or to infinite stresses in void elements [14]. This issue is addressed by using a stress criterion that is independent of the design variables and later combined with a vanishing constraint which also solves the singular optima problem discussed in Section 3.2. In doing so, the maximum Young's modulus is used to compute the stress criteria, even if the considered element is grayscale or void, following [37,47].

3.1.1. Stress constraint

The resulting "local" Cauchy stress tensor in Voigt notation is derived based on Eq. (2)

$$\boldsymbol{\sigma} = \frac{1}{J}\boldsymbol{F}\boldsymbol{S}\boldsymbol{F}^{\mathrm{T}}, \tag{48}$$

where the second Piola-Kirchhoff stress tensor $\boldsymbol{S}$ is evaluated at the Gauss points based on the Lame material parameters of the solid material, i.e. the Young's Modulus of each stress constraint is set to $E_{\max}$. Next, the von Mises yield criterion

$$\sigma^{\mathrm{v}} = \sqrt{\boldsymbol{\sigma}^{\mathrm{T}}\boldsymbol{V}_0\boldsymbol{\sigma}} \tag{49}$$

with

$$\text{in 2D: } \boldsymbol{V}_0 = \begin{bmatrix} 1 & -0.5 & 0 \\ -0.5 & 1 & 0 \\ 0 & 0 & 3 \end{bmatrix} \tag{50}$$

is used to compute a density-independent scalar stress measure for each element. Thus, the element-wise stress constraint of Eq. (47) is

$$g_j = \frac{\sigma_j^{\mathrm{v}}}{\sigma^{\mathrm{lim}}} - 1 \leq 0, \tag{51}$$

where σ^{lim} is the predefined stress limit. Note that the von Mises yield criterion for each element σ_j^v is obtained by evaluating the von Mises yield criterion at all Gauss points of the element and taking the average. Additionally, the stress constraint should vanish for void elements, which is why, the stress constraint of Eq. (51) must be transformed into a vanishing constraint. The used vanishing constraints will be introduced in the following Sections.

3.1.2. Stress limit

Both commonly used strategies for stress-constrained topology optimization, i.e. aggregation and the augmented Lagrangian approach, suffer from a low convergence rate close to a feasible design. As for near-optimal designs most stress constraints are fulfilled and the remaining active stress constraints mostly have small values. Therefore, the gradients of the stress constraints are flat, while the gradients of the mass objective remain constant. Consequently, the optimizer tends to further minimize the mass instead of satisfying the active constraints. This problem is usually solved with a simple workaround in which the stress limit of the stress constraints of Eq. (51) is chosen as $\widetilde{\sigma}_{\mathrm{lim}} < \sigma_{\mathrm{lim}}$, while the original stress limit σ_{lim} is used to identify valid designs. In doing so, the gradients of active stress constraints are steeper near optimal points, which speeds up the convergence significantly.

3.2. Singular optima

Global optima in optimization problems subject to stress constraints are typically located in degenerate regions of lower dimension than the problem domain. This was first discovered by [45] when performing structural optimization of truss structures with local stress constraints. The optimizer used was unable to find the known globally optimal design.

Standard optimization techniques are unable to find singular optima as long as the enforcement of constraints is based on Karush-Kuhn-Tucker conditions. This is because the Slater condition is not met for stress constraints in degenerate regions, so that the constraint qualification is not valid [6]. Thus, the KKT conditions no longer provide necessary and sufficient conditions for optimality [7].

The most common solution to this problem is to use a relaxed stress measure like the ϵ-relaxation [12] or the qp-relaxation [8] to increase the dimension of the degenerate regions. However, these approaches slightly modify the optimization problem and usually require solving the problem iteratively while decreasing the relaxation parameter.

More recently, the singular optimality problem is solved using piecewise vanishing constraints. This method has been successfully applied to stress constraints using aggregation functions [47] as well as using the augmented Lagrangian approach [37]. Here, the optimizer only receives information about stresses computed for the solid domain and the piecewise vanishing constraint removes the discontinuity of the stresses for $\varphi_j \to 0$. While the used P-mean aggregation function includes a relaxation of the stresses and therefore the constraint qualification remains valid, the augmented Lagrangian approach does not depend on KKT conditions to enforce the stress constraints. Consequently, both approaches combined with suitable filtering allow finding designs that are located in degenerate regions and that are close to a fully "0–1" design. Note that a relaxed stress measure is still needed to evaluate the end criteria of the optimization as long as no fully binary design is found. For this purpose, a qp-relaxation is used to approximate the stress inside non-binary finite elements.

3.3. Augmented Lagrangian approach

The augmented Lagrangian approach is widely used to deal with stress constraints in topology optimization [11,15,25,37,55] and has been shown to be capable of solving large-scale problems [13]. Using this approach, the stress constraints are moved into the objective of the optimization problem, where the objective is augmented by a penalty term $P^{(k)}$. Thus, the number of constraints is significantly reduced. However, the augmented Lagrangian approach can only be applied to equality constraints so the stress constraints $g_j \leq 0$ must be transformed into equality constraints $h_j = 0$. Furthermore, a cubic vanishing constraint has proven to be a good choice for the augmented Lagrangian approach [22] addressing the challenges discussed previously, in Sections 3.1 and 3.2. The cubic vanishing constraint reads

$$\theta_j = \varphi_j^p \left(g_j^3 + g_j \right) \leq 0. \tag{52}$$

In doing so, the original optimization problem Eq. (47) is replaced by a series of k less constrained suboptimization problems

$$\min_{\boldsymbol{\varphi}} \mathcal{L}^{(k)}(\boldsymbol{\varphi}) = m(\boldsymbol{\varphi}) + \underbrace{\frac{1}{n_{\mathrm{el}}} \sum_{j=1}^{n_{\mathrm{el}}} \left[\lambda_j^{(k)} h_j + \frac{\mu^{(k)}}{2} h_j^2 \right]}_{P^{(k)}}$$

$$\text{s.t.} \begin{cases} \boldsymbol{r}(\boldsymbol{\varphi}, \boldsymbol{x}) = \boldsymbol{0} \\ \boldsymbol{0} \leq \boldsymbol{\varphi} \leq \boldsymbol{1} \end{cases} \tag{53}$$

where only the contact residual $\boldsymbol{r}$ and the SIMP constraint remain as constraints of the optimization problem, while all stress constraints are moved to $P^{(k)}$. In doing so, the Lagrange multiplier $\lambda_j^{(k)}$ and the penalty factor $\mu_j^{(k)}$ are introduced. In theory, each suboptimization problem must be solved until convergence is observed. However, numerical studies reveal that solving each suboptimization problem for only 20 iterations is sufficient in practice [40]. Furthermore, the equality constraints of the vanishing stress constraint of Eq. (52) are

$$h_j = \max\left(\theta_j, -\frac{\lambda_j^{(k)}}{\mu^{(k)}}\right). \tag{54}$$

The parameters $\lambda^{(k)}$ and $\mu^{(k)}$ are kept constant for each suboptimization problem and they are initialized with $\lambda^{(1)} = \boldsymbol{0}$ and $\mu^{(1)} = 100$. The update rule after each suboptimization problem is given by

$$\lambda_j^{(k+1)} = \lambda_j^{(k)} + \mu^{(k)} h_j, \tag{55}$$

$$\mu^{(k+1)} = \alpha \mu^{(k)}. \tag{56}$$

The numerical factor $\alpha > 1$ is used to control the increase of the penalty factor. In addition, the penalty term is normalized to the number of stress constraints. Thus, the objective-to-penalty ratio is less dependent on the discretization, and adjusting $\lambda^{(1)}$ and $\mu^{(1)}$ is usually avoided when refining the discretization [37].

3.3.1. Extended augmented Lagrangian approach

The numerical results of the upcoming Sections 5 and 5.2.3 will reveal that the contact-constrained topology optimization will sometimes fail if the presented augmented Lagrangian approach is used. More precisely, the stresses of a few elements located at the contact surface converge to a stress significantly higher than the imposed stress limit. Thus, the gradient-based optimization does not find a way to improve the performance of these elements. Consequently, the presented approach should be adapted for contact problems.

To address this issue, an extended augmented Lagrangian approach is proposed to improve the satisfaction of the stress constraints for elements located in the vicinity of the contact interface, hereafter referred to as contact elements. These areas are often critical since occurring contact pressures have to be transferred between structures. The main idea is to guide the optimization early towards a more constraint-compliant design at the contact elements. This is accomplished by introducing a second augmented Lagrangian term

$$\mathcal{L}_{\mathrm{c}}^{(k)}(\boldsymbol{\varphi}) = \frac{1}{n_{\mathrm{ce}}} \sum_{l=1}^{n_{\mathrm{ce}}} \left[\lambda_l^{(k)} h_l + \frac{\mu^{(k)}}{2} h_l^2\right], \tag{57}$$

that considers only the stress constraints of the contact elements. In Eq. (57), n_{ce} denotes the total number of contact elements in the problem domain. As long as the elements at the contact surfaces violate the stress constraint, the design update is biased towards these elements. Once all stress constraints in the vicinity of the contact surfaces are satisfied, the additional Lagrangian contribution vanishes, and the standard augmented Lagrangian formulation for stress-constrained optimization is retained. The extended Lagrangian is given by combining Eq. (57) and $\mathcal{L}^{(k)}$, see Eq. (53), yielding

$$\widetilde{\mathcal{L}}^{(k)}(\boldsymbol{\varphi}) = \mathcal{L}^{(k)}(\boldsymbol{\varphi}) + \mathcal{L}_{\mathrm{c}}^{(k)}(\boldsymbol{\varphi}), \tag{58}$$

which can be written in more compact form by introducing the parameter for the j-th element

$$w_j = \begin{cases} 1 + \dfrac{n_{\mathrm{el}}}{n_{\mathrm{ce}}} & \text{, if the } j\text{-th element is part of any contact surface} \\ 1 & \text{, else} \end{cases} \tag{59}$$

where n_{ce} denotes the total number of elements in the problem domain. In doing so, the extended Lagrangian can be rewritten to

$$\widetilde{\mathcal{L}}^{(k)}(\boldsymbol{\varphi}) = m(\boldsymbol{\varphi}) + \underbrace{\frac{1}{n_{\mathrm{el}}} \sum_{j=1}^{n_{\mathrm{el}}} w_j \left[\lambda_j^{(k)} h_j + \frac{\mu^{(k)}}{2} h_j^2\right]}_{\widetilde{P}^{(k)}}. \tag{60}$$

Consequently, violations of the stress constraints at the contact surfaces have a stronger influence on the design update. In practical applications, this encourages the optimizer to prioritize satisfying the stress constraints at the contact surfaces during the first few subproblems, avoiding the observed convergence problems of the standard augmented Lagrangian approach.

This extension avoided the optimizer becoming stuck in an infeasible local minimum during our employed optimizations. However, one should always start with the standard augmented Lagrangian approach and only restart using the extended augmented Lagrangian approach if the optimizer becomes stuck in such an infeasible local minimum. The extended approach does not require an additional tuning parameter, yet it might lead to numerical problems if the ratio of $n_{\mathrm{el}}/n_{\mathrm{ce}}$ becomes too large.

3.4. Aggregation stress constraints

Alternatively to the local approach of Eq. (53), the optimization problem of Eq. (47) can be reformulated using the max-function

$$\min_{\boldsymbol{\varphi}} m(\boldsymbol{\varphi}) = \frac{1}{v_{\mathrm{t}}} \sum_{i=1}^{n_{\mathrm{el}}} v_i \varphi_i$$
$$\text{s.t.} \begin{cases} \max(g_1, \ldots, g_{n_{\mathrm{el}}}) \leq 0 \\ \boldsymbol{r}_{\mathrm{c}}(\boldsymbol{\varphi}, \boldsymbol{x}) = \boldsymbol{0} \\ \boldsymbol{0} \leq \boldsymbol{\varphi} \leq \boldsymbol{1} \end{cases} \tag{61}$$

In doing so, the number of stress constraints is reduced to a single stress constraint which looks appealing from an optimization point of view, as the gradient of only a single constraint is significantly cheaper. However, the max-function is non-differentiable which is why an aggregation function is usually used to approximate the max-operator. This procedure is commonly used in the field of stress-constrained topology optimization; see e.g.[21,27,40,47].

This work follows the unified aggregation and relaxation approach of [47] as an explicit relaxation technique is not required. In doing so, the max-function is approximated by the P-mean function which is a lower bound approximation. Additionally, a linear vanishing constraint is used

$$\Theta_j = \varphi_j g_j \leq 0, \tag{62}$$

so that the resulting unified aggregation and relaxation approach reads

$$\min_{\boldsymbol{\varphi}} m(\boldsymbol{\varphi}) = \frac{1}{v_{\mathrm{t}}} \sum_{i=1}^{n_{\mathrm{el}}} v_i \varphi_i$$
$$\text{s.t.} \begin{cases} \Psi = \left(\dfrac{1}{n_{\mathrm{el}}} \sum\limits_{j=1}^{n_{\mathrm{el}}} (\Theta_j + 1)^P\right)^{(1/P)} - 1 \leq 0 \\ \boldsymbol{r}_{\mathrm{c}}(\boldsymbol{\varphi}, \boldsymbol{x}) = \boldsymbol{0} \\ \boldsymbol{0} \leq \boldsymbol{\varphi} \leq \boldsymbol{1} \end{cases} \tag{63}$$

In Eq. (63), the aggregation parameter is $P > 0$ which simultaneously controls the required relaxation. The effect of this relaxation is discussed in detail in [47]. If the aggregation parameter $P \to \infty$, then Eq. (63) equals Eq. (61) and thus, the actual mass minimization problem of Eq. (47) is considered. In practice, a significantly smaller aggregation parameter is used (usually $P << 60$), since the aggregated stress constraint becomes increasingly difficult to handle numerically as the aggregation

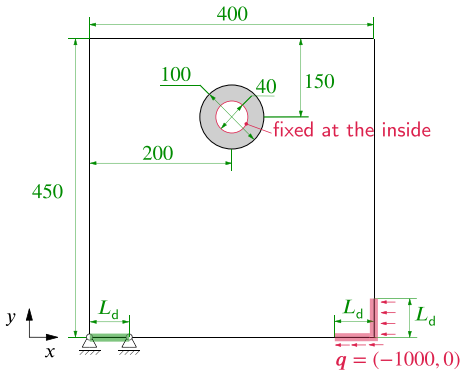

Fig. 5. Modified benchmark example of [43] with uniformly distributed load q and sliding bearing. Both are distributed over the length $L_d = 30$. All lengths are in millimeters, and the total load is given in Newtons.

parameter increases. In the literature, convergence problems for $P > 60$ are well documented, see e.g. [47], which is why, a ramp up strategy for the aggregation parameter during the optimization is followed, see [40]. This allows for further increasing the aggregation parameter. However, at a certain magnitude of the aggregation parameter, divergence of the optimization is still observed.

4. Influence of the different contact models on the stress computation

In order to perform stress-constrained topology optimization successfully, the influence of the contact constraints and contact coupling techniques of Section 2 on the resulting stress fields is analyzed for a given design first. Although the effects of contact discretization on the stresses are well documented in the finite element contact mechanics literature, their implications for stress-constrained topology optimization have not been investigated. For the stress analysis, the contact constraints will be imposed using either the presented Lagrange Method, where the *Hertz-Signorini-Moreau* condition (HSM) is exactly satisfied, or using the unilateral penalty (UP) method. To show the influence of the penalty factor on the optimization and the stress computation, two penalty factors are considered. Computations based on a unilateral penalty factor of $\epsilon_N = 1e3$ are labeled with UP1, while UP2 is used for a penalty factor of $\epsilon_N = 1e4$.

The analysis is based on a modified version of the benchmark of Strömberg and Klarbring [43]. The design domain is shown in Fig. 5. This benchmark was introduced only for unilateral boundary constraints, meaning that the inner contact support is modeled using geometric constraints. Thus, the inner support was undeformable. Using the presented methods, deformable contact supports are also considered, and the inner contact support is replaced by a disc-like structure, which is fixed on the inside. In doing so, the design domain is discretized into 11132 quadrilateral finite elements, while the contact support is discretized into 1206 quadrilateral elements. The finite element discretizations are chosen so that the discretizations at the contact surfaces are non-matching as this cannot be guaranteed in practice. In doing so, the contact surface of the design domain is discretized with 80 segments, while the contact surface of the inner disc is discretized with 116 segments. The Young's Modulus of the design domain and the contact support is 210000 MPa and a compressible Neo-Hookean material model is used, see Eq. (4).

For demonstration purposes, a previously compliance-optimized design is used to compute the stresses under all combinations of contact constraints and the contact coupling techniques. Note that for this comparison, the previously compliance-optimized design has been obtained based on the framework of [43], which uses a node-to-segment contact coupling combined with the HSM contact condition and the inner disc is considered rigid. However, for comparison of the contact modeling methods, the inner disc is now also considered deformable. The volume of the given design is 30% of the total volume.

The stress fields obtained without blending the discretized contact surfaces to the exact geometry are shown in Fig. 6. The maximum stress differs for the contact formulations and the overall stress distributions vary significantly. In addition, the stresses obtained with HSM and the higher penalty factor UP2 exhibit non-smooth oscillating behavior near the contact interface when the node-to-segment coupling is used. For the segment-to-segment coupling, all three contact formulations yield a comparable maximum stresses and similar overall stress distributions. However, the non-smooth behavior of the stresses near the contact interface is still observed for HSM and UP2.

In contrast, Fig. 7 shows the stress fields obtained when the discretized contact surfaces are blended to the exact geometry. Overall, the maximum stresses are in much better agreement, except for UP1 in combination with the node-to-segment coupling. The same observation applies to the overall stress distributions. For HSM and UP2, both the node-to-segment and the segment-to-segment coupling lead to similar stress fields. Moreover, no rapidly varying stresses are observed near the contact interface.

This is expected, since these stress oscillations near the contact interface are artificial and are caused by the discretization of the contact surfaces as described in Section 2.4. The root of the artificial stresses in the vicinity of the contact surface can be traced back to an inaccurate distribution of the contact pressure. This is demonstrated in Fig. 8, where the contact pressure is visualized along the contact surface for non-blended and blended contact surfaces. The Fig. 8(a) and (b) show the contact pressure using the node-to-segment and segment-to-segment contact without blending, whereas the Fig. 8(c) and (d) use the circular blending function to accurately model the contact surface geometry. The influence of the blending approach is clearly visible in the contact pressure distribution. Without the circular blending function, the contact pressure shows pronounced oscillations, whereas a smoother distribution is obtained when blending is applied. However, even with blending, some oscillations remain when the node-to-segment coupling technique is used. These oscillations are not observed when using the segment-to-segment approach. This can be attributed to the different evaluation of the contact pressure. For the segment-to-segment approach, the contact potential containing the contact pressure is defined by an integral over the whole contact surface (see Eq. (37)), which is typically discretized for every secondary segment using a high-order quadrature rule. In contrast, the contact potential for node-to-segment coupling considers only the contact pressure evaluated at the nodes of the secondary contact surface (see Eq. (18)). As a result, the segment-to-segment approach represents the contact pressure more accurately in comparison to the node-to-segment approach when evaluated using the same spatial discretization. Therefore, the segment-to-segment approach provides more accurate contact pressure distributions for coarser discretizations of the contact surfaces while also being less prone to artificial stress oscillations induced by the discretization error of the contact surface geometries. This is particularly relevant for efficient contact- and stress-constrained topology optimization, since refining the discretization of the contact surfaces increases both the number of contact constraints and stress constraints as well as increasing the number of design variables.

The necessity of exact modeling of the contact surfaces has not yet been discussed in the context of contact-constrained topology optimization [16,42]. This is because stresses on curved contact surfaces have not been considered for node-to-segment or segment-to-segment coupling, and the differences between the optimized designs for objective functions such as the compliance are rather small. This is demonstrated in the Appendix B, where compliance-optimized designs with and without applying a circular blending function are shown. However, the effect of these artificial stress peaks on a mass minimization problem is not negligible as the optimizer has to find a way to reduce these stress peaks.

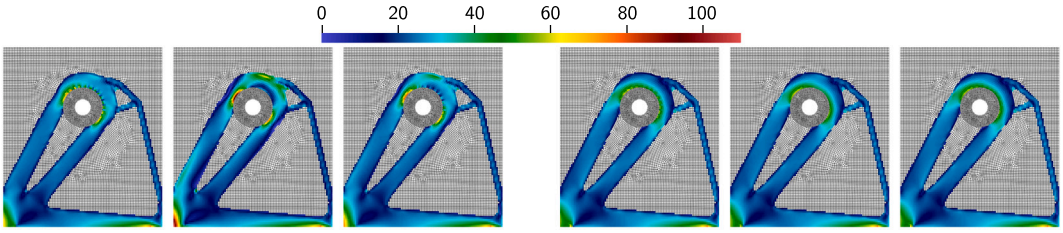

(a) n2s-HSM, $\sigma_{max} = 74.5$. (b) n2s-UP1, $\sigma_{max} = 109.3$. (c) n2s-UP2, $\sigma_{max} = 77.3$. (d) s2s-HSM, $\sigma_{max} = 74.0$. (e) s2s-UP1, $\sigma_{max} = 74.1$. (f) s2s-UP2, $\sigma_{max} = 74.0$.

Fig. 6. Stress fields of a given design with a deformable contact support for different contact coupling techniques and contact constraints. Only elements with a density greater than 20% are shown.

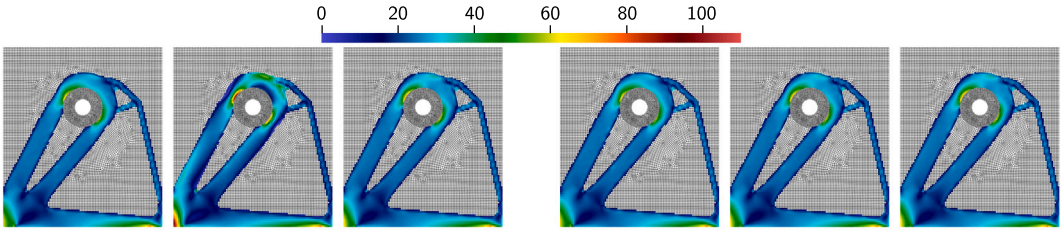

(a) bl. n2s-HSM, $\sigma_{max} = 74.2$. (b) bl. n2s-UP1, $\sigma_{max} = 100.3$. (c) bl. n2s-UP2, $\sigma_{max} = 74.4$. (d) bl. s2s-HSM, $\sigma_{max} = 74.2$. (e) bl. s2s-UP1, $\sigma_{max} = 74.7$. (f) bl. s2s-UP2, $\sigma_{max} = 74.4$.

Fig. 7. Stress fields of a given design with a deformable contact support and blending for different contact coupling techniques and contact constraints. Only elements with a density greater than 20% are shown.

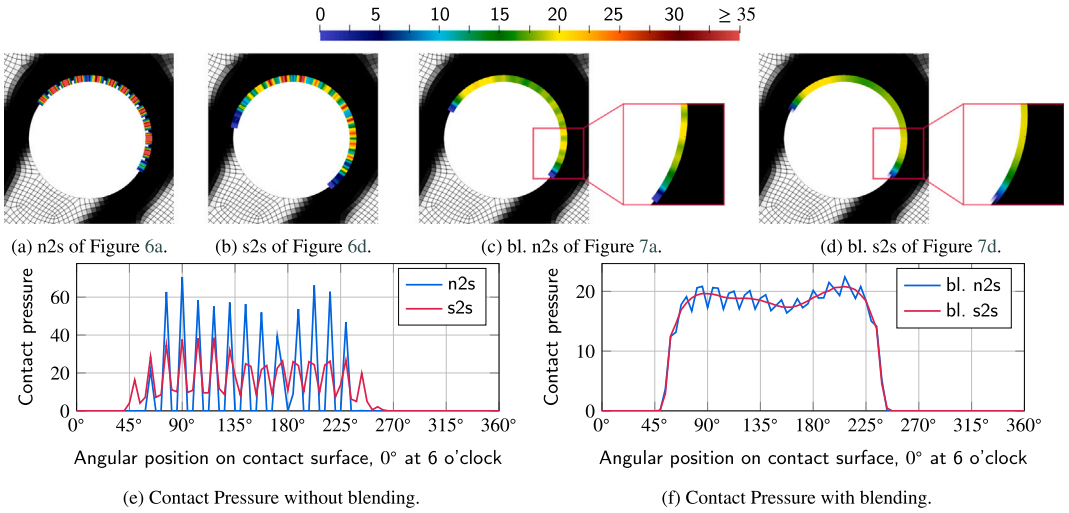

Fig. 8. Contact pressure in MPa along the contact surface of the design space for non-blended and blended ('bl.') contact surfaces using the Hertz-Signorini-Moreau (HSM) contact constraint.

The effect of not using blending functions in stress-constrained mass minimization is demonstrated in Appendix C.

In summary, evaluating the different stress fields of the previously given compliance-optimized design reveals that accurately modeling the contact surfaces is crucial for meaningful results in stress-constrained topology optimization. Otherwise, the stress field in the vicinity of the contact will be dominated by artificial stress peaks that occur due to a scattered contact pressure along the contact surface. Furthermore, the penalty factor of the unilateral penalty method must be sufficiently high and validated before optimization. In this example, UP1 with a penalty factor of $\epsilon_N = 1e3$ is insufficient. Consequently, the next section will only consider deformable contact supports that are blended if curved contact surfaces are considered.

5. Stress-constrained mass minimization

In this section, three different benchmark problems for stress- and contact-constrained mass minimization problems will be discussed. In doing so, the mass minimization problem of Eq. (47) is either replaced by the optimization problem using the augmented Lagrangian approach or the P-mean aggregation for the stress constraints. Furthermore, the influence of the different contact constraints (see Section 2.2) and contact coupling techniques (see Section 2.3) is discussed.

The first Section 5.1 deals with a benchmark example that was introduced by [43] in the context of contact-constrained compliance topology optimization and was also considered in the previous section. The second Section 5.2 deals with a modified L-shaped design domain, which is commonly used in stress-constrained topology optimization and modified

Table 1
Parameters for the optimization of the Lug.

Stress limits	
σ_{lim}	60 MPa
$\widetilde{\sigma}_{\text{lim}}$	$0.99 \cdot \sigma_{\text{lim}} = 59.4$ MPa
Density filter	
r_{min}	15
Projection filter	
η	0.5
β_{start}	1.0
β_{max}	5.0
β_{increase}	1.0341
Optimizer	
uniform initial density	0.6
move limit	0.05
maximum iterations	1000
iterations per suboptimization	20
Aggregation	
P_{start}	20
P_{max}	20, 100 or 200
P_{increase}	1.0,1.0341 or 1.04914
Augmented Lagrangian Approach	
μ_{start}	100
μ_{max}	13,150
α	1.05

for contact. The last Section 5.3 demonstrates the simultaneous optimization of two structures that are in contact and are undergoing large deformations.

5.1. Curved contact surface - the Lug

In the following, the stress-constrained mass minimization problem is applied to the modified benchmark example of Strömberg and Klarbring [43] of Fig. 5 using a compressible Neo-Hookean material model; see Eq. (4). The optimizations are performed with either the augmented Lagrangian approach of Eq. (53) or the mass minimization problem using stress aggregation of Eq. (63). Furthermore, a density filter and a projection filter [48] are employed. The parameters used are shown in Table 1. In doing so, the mass minimization process is subdivided into suboptimization problems with constant stress constraint parameters. More precisely, the stress constraint parameters are the Lagrange multiplier λ of Eq. (55) and the penalty parameter μ of Eq. (56) if the augmented Lagrangian approach of Eq. (53) is used. Otherwise, the optimization problem based on aggregation is considered, and the stress constraint parameter is the aggregation order P. For both optimization problems, the projection filter and the stress constraint parameters are updated after each suboptimization problem according to the increase factors. The increase factors β_{increase} and P_{increase} in Table 1 are chosen such that the maximum values are reached after 980 iterations, which is similarly done by [40]. Please note that this does not apply to the augmented Lagrangian penalty factor μ, which increases after each suboptimization problem until the maximum number of iterations is reached or a feasible design is found. Once again, both node-to-segment (n2s) and segment-to-segment (s2s) contact coupling are considered. Based on the prior discussion regarding an accurate modeling of the contact surfaces, see Section 4, a circular blending function is used on both contact surfaces. In doing so, it is guaranteed that the optimized designs are not affected by stresses that occur only due to the chosen discretization at the contact surfaces.

This is essential because, without blending, much finer meshes would be necessary during optimization to prevent artificial stress peaks near the contact surface. However, employing a finer mesh would greatly increase computational costs, since stress-constrained topology optimization typically demands numerous iterations to obtain feasible designs. This is further discussed in the Appendix C, which also contains numerical results without blending.

5.1.1. Augmented Lagrangian approach

In this section, the augmented Lagrangian approach as presented in Section 3.3 is used to solve the stress-constrained mass minimization problem. The optimized designs as well as the convergence history are shown in Fig. 9. The shown optimized designs are the lightest designs found that still satisfy the stress limit of 60.0 MPa. In fact, several designs in each optimization satisfy the stress constraint. The first feasible designs are marked in the stress history of Fig. 9 with ■ for s2s and ▲ for n2s. These are obtained between iterations 480 and 650, while the best performing designs are found around 1000 iterations. Furthermore, Table 2 provides additional information on the shown designs.

All of the obtained optimized designs are feasible and fulfill the applied constraints. The best performing designs have a similar mass between 18.8% and 19.6%, except for the design obtained using the penalty factor UP1 for the n2s coupling which is significantly heavier. Here, there is extra material located near the contact surface. Also, the elements near the contact surface exhibit intermediate densities despite the applied filtering. Overall, the designs obtained using HSM can be seen as a reference solution for n2s and s2s contact coupling techniques because the HSM constraint strictly enforces the contact conditions. Consequently, the contact modeling using the HSM constraint is the most accurate. Both designs found using HSM are basically identical and have the nearly identical mass. However, the designs found using the penalty-based constraints vary in mass or mass distribution compared to the designs found by HSM. Yet, all designs are feasible from an optimization point of view.

5.1.2. Aggregation

In this Section, the P-mean aggregation function is used to handle the stress constraints and therefore, the optimization problem of Section 3.4 is solved. In doing so, three different maximum aggregation values $P_{\text{max}} = \{20, 100, 200\}$ are applied. In this Section, only HSM contact constraint will be considered, as the results of the former Section have shown the influence of the too low penalty factor UP1 in stress-constrained topology optimization subjected to contact. If aggregation is used, similar effects are observed as the inaccurate contact modeling dominates the stress distribution and therefore, also dominates the aggregation function.

The resulting designs and the convergence history are shown in Fig. 10 and additional data about the optimized designs are shown in Table 3. It is worth mentioning that the optimized designs using n2s and s2s contact-coupling are rather similar for this specific example.

As expected, the results show that the imposed stress limit of 60.0 MPa is not reached, since the P-mean function is a lower-bound approximation of the max-function. Consequently, aggregation based on the P-mean function will underestimate the actual maximum stress within the design domain. That being said, the lowest maximum aggregation $P_{\text{max}} = 20$, see Fig. 10(a) and (d), is not suitable as the maximum stress is more than 25% above the imposed stress limit. Looking at the optimized designs with the $P_{\text{max}} = 100$, see Fig. 10(b) and (e), the maximum stress of the optimized designs is still 6% above the stress limit, while the total mass of the design slightly exceeds the mass of the feasible designs obtained using the augmented Lagrangian approach, which has been presented in the former section. Thus, the usage of higher aggregation parameters reduces the difference between the maximum stress inside the design domain and the imposed stress limit at the cost of an increasing mass, see Table 3. Yet, higher aggregation parameters $P_{\text{max}} = 200$ seem to destabilize the optimization process after a certain number of iterations, which can be seen in the convergence histories of Fig. 10. This can be seen in the optimization based on n2s contact-coupling with $P_{\text{max}} = 200$. After iteration 961, the maximum stress

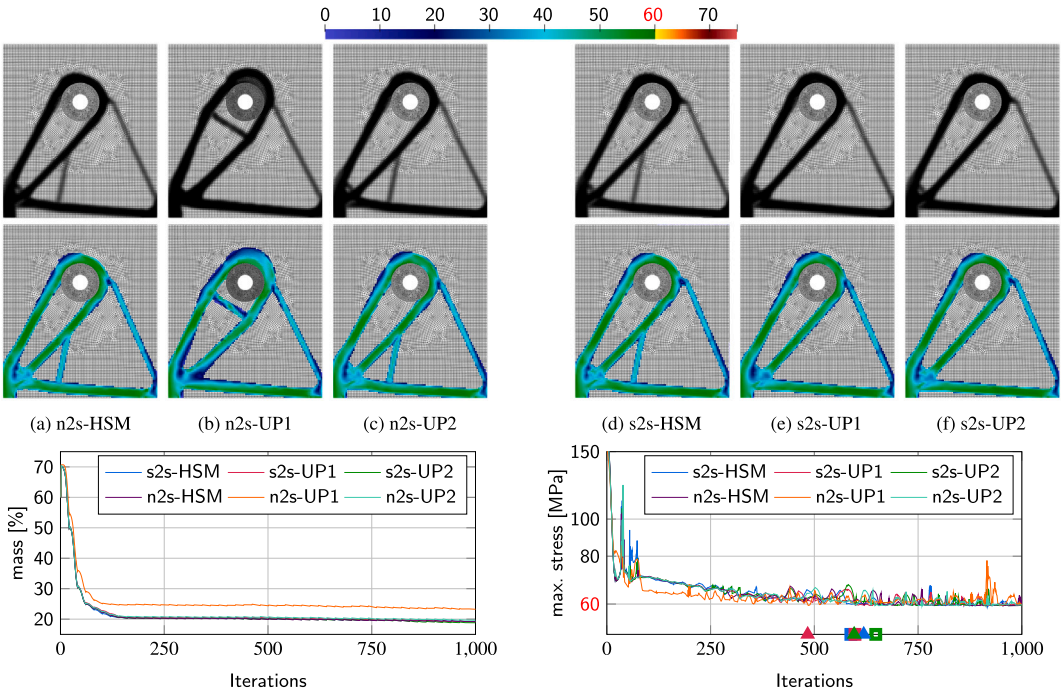

Fig. 9. Best optimized designs in deformed configuration and convergence history using the augmented Lagrangian approach with blending functions. The first design reaching the stress limit is marked, ■ s2s & ▲ n2s.

Table 2
Details about the best performing designs - shown in Fig. 9 - obtained using the augmented Lagrangian approach.

Coupling	Constraint	Iterations	Mass [%]	Maximum stress [MPa]
n2s	HSM	997	19.2	60.0
	UP1	961	23.2	60.0
	UP2	992	19.6	59.7
s2s	HSM	980	19.2	59.6
	UP1	998	19.1	59.7
	UP2	997	18.8	59.6

increases drastically which causes the later rise observed in the mass plot and results in unusable designs after 1000 iterations. It appears that the high aggregation parameter $P_{\max} = 200$ causes the gradient-based design update to concentrate primarily on the most critical stress elements. As a result, the stresses in other elements receive less attention during the design update, which can destabilize the optimization process. This effect may be amplified by the non-smooth characteristic of the contact problem because changes in the design can significantly alter the contact surface, which dominates the stress distribution in the vicinity of the contact surface. In consequence, the shown design of Fig. 10(c) is obtained before the jump in the stress constraint is observed.

5.1.3. Concluding remarks

First, accurately modeling the geometry at the contact surfaces is key to accurately calculating stresses at those surfaces. This is important because an insufficient contact pressure dominates the stresses in the vicinity of the contact surface, which in turn will mislead the optimization. Consequently, the chosen discretization of the contact surfaces must not dominate these stresses. One way to address this challenge is to use finer meshes to improve the accuracy of the stress computation. However, mesh refinement substantially increases the computational cost per optimization iteration, since it increases both the size of the system equations and the total number of stress constraints. Additionally, stress-constrained optimization may require several hundred to a few thousand iterations to achieve a feasible design, which is why using finer discretizations should be a last resort. This can be circumvented using techniques such as applying blending functions, where the geometry of the contact surfaces is exactly modeled without introducing further degrees of freedom or design variables.

From an optimization perspective, both node-to-segment and segment-to-segment coupling techniques can be used, as both result in reasonable designs in this example. From a contact mechanics perspective, however, segment-to-segment methods are superior because they compute the most realistic contact pressure and pass the patch test [31]. Finally, if a penalty approach is considered, the penalty values must be sufficiently high. Otherwise, the optimization will exploit this false model assumption, resulting in a poorly performing design.

5.2. Planar contact surfaces - the L-Bracket

The following section discusses a modified L-Bracket. The L-Bracket is a benchmark example of stress-constrained topology optimization and has been discussed in detail in the literature; see, for example [21,40,47]. In contrast to the standard L-Bracket, a nonlinear contact problem is considered. Thus, physical material parameters as well as dimensions have to be chosen. The presented example is closest to [21], where physical material parameters and dimensions are also chosen. The L-Bracket is visualized in Fig. 11 and the parameters used are shown in Table 4. Once again, a compressible Neo-Hookean material model is used; see Eq. (4). The former numerical example already discussed the influence of directly applying the *Hertz-Signorini-Moreau* (HSM) contact conditions using a Lagrange method and the influence of approximating these conditions using a unilateral penalty method. Therefore, this section will only deal with the HSM contact constraint as it provides a more accurate modeling of the contact conditions. Additionally, only segment-to-segment contact coupling is used, as the influence of n2s and s2s contact coupling has already been discussed in depth in the prior sections.

Only the L-Bracket will be considered as design space; however, the three contact supports are deformable. The design domain is discretized by 25600 finite elements, while the vertical supports are discretized by 720 finite elements, and the horizontal boundary is discretized by 256

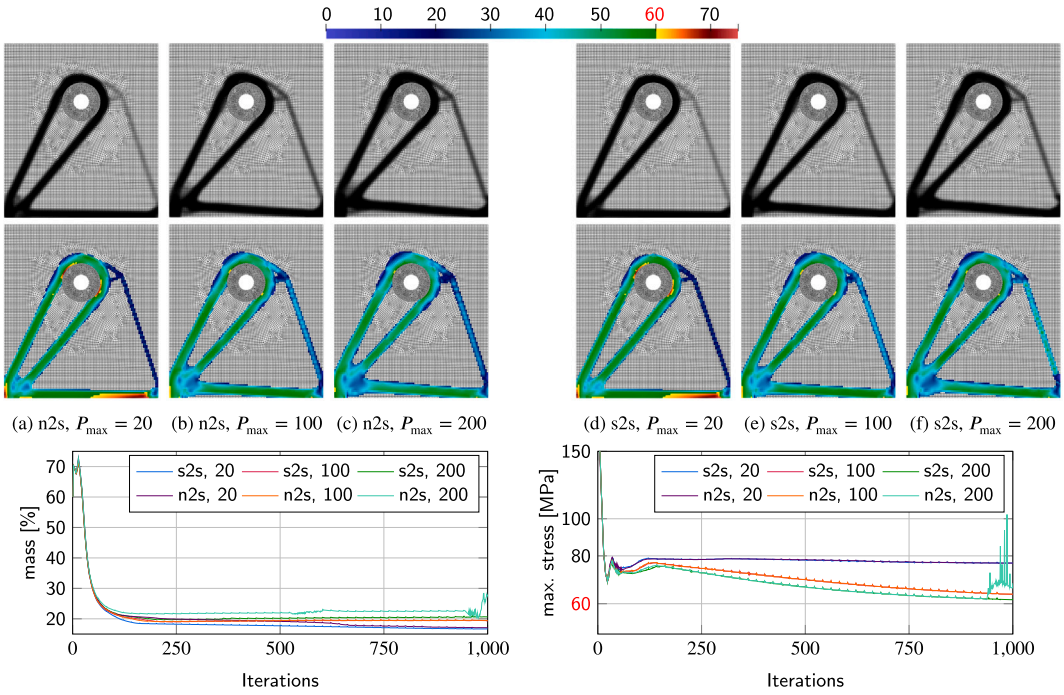

Fig. 10. Best optimized designs in deformed configuration and convergence history using aggregation with blending functions. The initial aggregation value is $P_{start} = 20$, and the final value reached after 980 iterations is $P_{max} = \{20,100,200\}$. All designs are obtained based on the HSM contact constraint.

Table 3
Details about the best performing designs - shown in Fig. 10 - obtained using aggregation. The initial aggregation is $P_{start} = 20$, the maximum at iterations 980 are $P_{max} = \{20,100,200\}$.

Coupling	Max. aggregation	Iterations	Mass [%]	Max. stress [MPa]
n2s	$P_{max} = 20$	1000	17.1	76.6
	$P_{max} = 100$	1000	19.5	63.6
	$P_{max} = 200$	961	20.4	61.9
s2s	$P_{max} = 20$	1000	16.7	76.6
	$P_{max} = 100$	1000	19.2	63.5
	$P_{max} = 200$	1000	20.0	61.4

finite elements. In this example, blending is not needed, as only straight contact surfaces are considered.

The used parameters of the stress-constrained mass minimization problem are shown in Table 5 and the overall procedure is unchanged from the former benchmark example in Section 5.1. In case of stress-constrained mass minimization using aggregation, the aggregation order gradually increased every 20 iterations starting from $P_{start} = 20$ to $P_{max} = 100$. The results of the stress-constrained mass minimization using the augmented Lagrangian approach (AL) and Aggregation (AGG) are discussed in the following. Afterward, the extended augmented Lagrangian approach (XAL) is demonstrated using a different setup of the L-Bracket.

5.2.1. Augmented Lagrangian approach

The optimized designs shown in Fig. 12(a) reveal that the augmented Lagrangian approach (AL) does result in a feasible design. However, the shown stress distributions in Fig. 12(a) only consider elements that have a density value greater than 20%, while the quantitative results presented in Table 6 and the convergence history reveal that the maximum qp-relaxed stresses without this threshold are significantly above the stress limit of 350 MPa. In order to visualize this problem, all elements that exceed the stress limit are colored red in the optimized designs of Fig. 12(a).

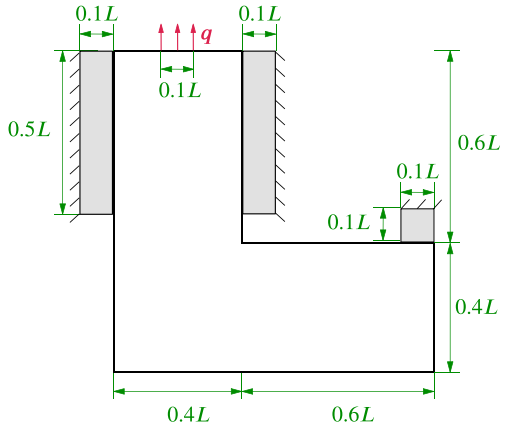

Fig. 11. L-Bracket with deformable contact support.

Table 4
Parameters of the L-Bracket.

Design Domains	
L	200 mm
E_{min}	1 MPa
E_{max}	71000 MPa
ν	0.33
Contact Supports	
E	10000 MPa
ν	0.33
Distributed Load	
q	(0, 1500 N)

This behavior is caused by the applied cubic vanishing constraints that suppress the influence of stresses in elements that are approaching the void phase. Consequently, elements with very low densities

Table 5
Parameters of the L-Bracket optimization.

Stress limits	
σ_{lim}	350 MPa
$\widetilde{\sigma}_{\text{lim}}$	$0.99 \cdot \sigma_{\text{lim}} = 346.5$ MPa
Density filter	
r_{min}	6
Projection filter	
η	0.5
β_{start}	0.1
β_{max}	3.464
β_{increase}	1.0766
Optimizer	
uniform initial density	0.6
move limit	0.05
maximum Iterations	1000
iterations per suboptimization	20
Aggregation	
P_{start}	20
P_{max}	100
P_{increase}	1.0341
Augmented Lagrangian Approach	
μ_{start}	100
μ_{max}	13,150
α	1.05

may exhibit large qp-relaxed stress values, while their corresponding vanishing-constraint values remain small. This does not indicate hidden failure points in load-bearing material, but rather reflects the fact that these elements have already lost almost all structural stiffness and are effectively part of the void phase. Eventually, the optimization usually finds a design that also satisfies the stress constraints in these void elements. However, these designs are typically much heavier in comparison and require many additional iterations.

Table 6
Details about the designs of Fig. 12 using the augmented Lagrangian approach (AL) and aggregation (AGG) with $P_{\text{max}} = 100$.

	Iterations	Mass [%]	Max. stress [MPa]	Max. stress with threshold [MPa]
AL	731	42.2	425.9	349.9
AGG	1000	50.1	364.3	364.3

The next paragraph discusses this phenomenon in depth.

Challenges with using a cubic vanishing constraint

The data of Table 6 shows the maximum stress values inside the design domain with and without the threshold, as the stress distribution in Fig. 12(a) only considers elements with a density value greater than 20%. In doing so, a qp-relaxation is used to visualize the stress inside non-binary finite elements. However, the qp-relaxation behaves differently from the cubic vanishing constraint, which is used during optimization. Due to that, especially elements with a density between 0.8% and 10% may have a qp-relaxed stress values that exceed the stress limit, while their corresponding influence on the Lagrangian is comparably small and likely gets lost in the noise of elements that just satisfy the stress limit. For improved convergence, the vanishing constraints used to compute the Lagrangian are computed with $\widetilde{\sigma}_{\text{lim}} = 0.99\sigma_{\text{lim}} = 346.5$ MPa a lower limit than the actual stress limit of $\sigma_{\text{lim}} = 350$ MPa. Thus in this example, any element with a solid stress value between 346.5 MPa and 350 MPa contributes to the Lagrangian, even though it satisfies the stress limit. This problem remains even after 1000 iterations, so introducing a threshold as [47] has used, significantly reduces the computational costs. Otherwise, in the presented example, about double the number of iterations is needed to find feasible designs.

Looking at the optimized design of iteration 731, which is the first design satisfying the stress limit using the threshold, the highest two qp-relaxed stress values of the optimized design have densities of $\varphi_1 = 5.3\%$ and $\varphi_2 = 8.5\%$, respectively. Both of these elements are located in a void region between two struts towards the tip of the L-Bracket. In order to compute the vanishing constraint, the von Mises stress based

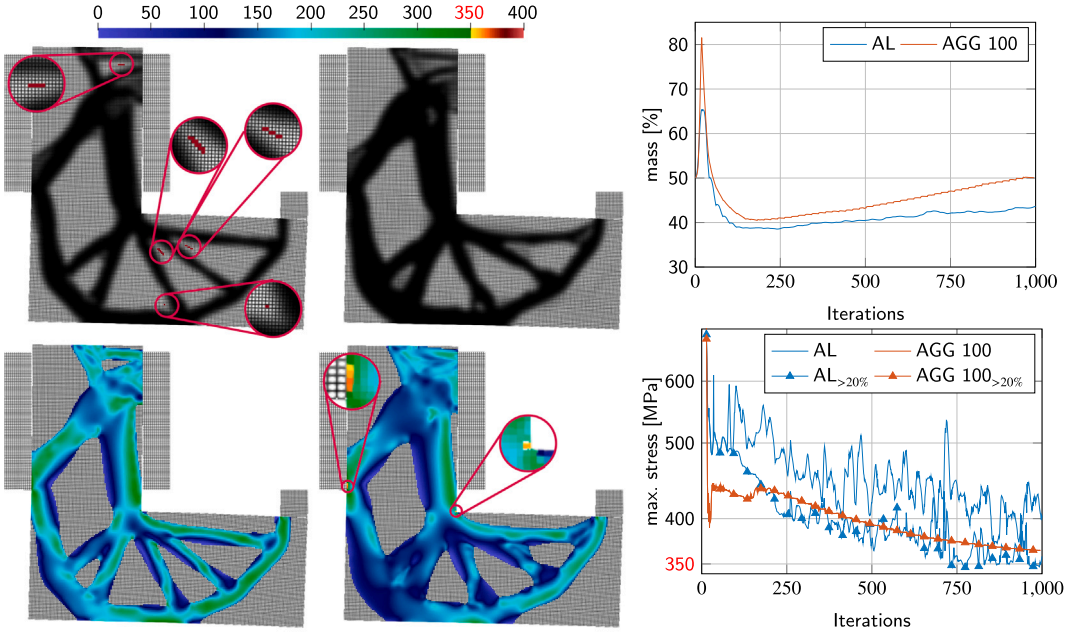

(a) AL (b) AGG 100

Fig. 12. Optimized designs in deformed configuration and convergence history using the augmented Lagrangian approach (AL) and aggregation with $P_{\text{max}} = 100$ (AGG 100). All designs are computed using s2s-HSM contact modeling. All elements with a density below 20% that do not fulfill the stress limit are marked in red. The additional maximum stress measure LP/AGG $100_{>20\%}$ only considers elements with a density $> 20\%$.

on the Young' Modulus of the solid material $E_{\max}$ is needed, which is $\sigma_1^{\mathrm{v}} = 1848.2$ MPa and $\sigma_2^{\mathrm{v}} = 1415.0$ MPa. The resulting qp-relaxed stress is then obtained by

$$\sigma_j^{\mathrm{qp}} = \sqrt{\varphi_j}\sigma_j^{\mathrm{v}} \rightarrow \begin{cases} \sigma_1^{\mathrm{qp}} = 425.9 \text{ MPa} > \sigma_{\lim}, \\ \sigma_2^{\mathrm{qp}} = 412.0 \text{ MPa} > \sigma_{\lim}. \end{cases} \tag{64}$$

However, the cubic vanishing constraint of Eq. (52) for both elements is $\theta_1 = 0.0128$ or $\theta_2 = 0.0198$, respectively. In order to put these numbers into perspective, a fictitious third element with a density of $\varphi_3 = 100\%$ and a solid von Mises stress of $\sigma_3^{\mathrm{v}} = 349.99$ MPa results in a cubic vanishing constraint value of $\theta_3 = 0.0111$, while its qp-relaxed stress is $\varphi_i^{\mathrm{qp}} = 349.99$ MPa. Note that the constraint for $\sigma_3^{\mathrm{v}} = 349.99$ MPa is still active as $\widetilde{\sigma}_{\lim} = 0.99\sigma_{\lim} = 346.5$ MPa is used to compute the vanishing constraint. Consequently, the influence on the Lagrangian of the two 'worst' elements and the fictitious third element has the same magnitude. Thus, the optimizer does not focus on void elements with too high qp-relaxed stresses and will focus about the same on each element that just satisfies the stress limit, which are in the majority for a close to optimal design. Thus, the optimization process is not driven by void elements exhibiting high qp-relaxed stresses. Rather, these stress constraints have about the same influence on the optimization as elements whose stresses are already below the target stress limit $\sigma_{\lim}$, yet above the imposed stress limit $\widetilde{\sigma}_{\lim} < \sigma_{\lim}$.

This is not a problem with the cubic vanishing constraint, of course. Rather, it is a problem of stress interpretation within non-binary finite elements that cannot be avoided when using a SIMP parameterization. This problem is visualized in Fig. 12, where the convergence history of the maximum stress and the maximum stress including the density threshold of 20% is shown, and clear differences are observed. Therefore, it is advisable to include a threshold if large stresses in void elements are observed, as the cubic vanishing constraints do not prioritize these elements. In this work a threshold value of 20% is used, as this value has also been used by [47]. However, smaller thresholds would also address this issue. Note that this problem does not occur in the first benchmark example of Section 5.1, as the void regions deform significantly less there.

5.2.2. Aggregation

In contrast to the augmented Lagrange approach, the optimized design computed based on aggregation performs significantly worse, as shown in Table 6, where the details about the optimized designs are listed. In fact, the optimized design using a maximum aggregation parameter of $P_{\max} = 100$ only reaches a maximum stress value of 364.3 MPa, while the design is about 20% heavier than the optimized design obtained by the augmented Lagrangian approach. It appears that the aggregation really struggles to reduce the stress peaks at the end of the left vertical contact surface as well as the stress singularity at the inside corner of the L-Bracket, see Fig. 12(b). As shown in the former example, lower maximum aggregation parameters could be used to obtain a lighter design, that is potentially closer to the optimized design of the AL approach. However, this comes at the cost of even higher violations of the stress constraints and vice versa, higher aggregation orders would further increase the mass, while improving the fulfillment of the stress constraints. Nevertheless, both options are not desirable, as the optimized design obtained by AL would always outperform the solution obtained by aggregation. Due to the linear vanishing constraint that is commonly used in aggregation, see [47], aggregation based optimization does not dismiss active stress constraints with a low density. Thus, the discussed challenges with using a cubic vanishing constraint are not observed. In consequence, there is no difference between the maximum stress with and without the threshold in Fig. 12.

5.2.3. Extended augmented Lagrangian approach

The following example considers a different L-Bracket setup with unilateral contact constraints. The design domain is shown in Fig. 13 and

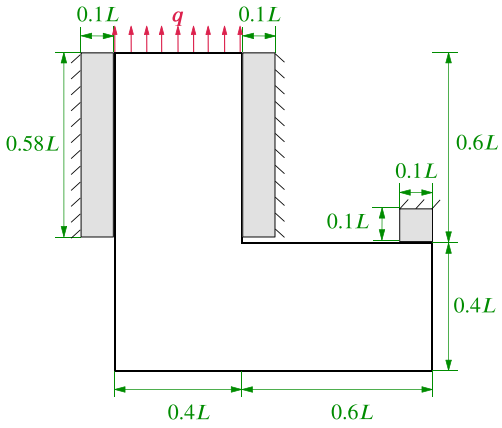

Fig. 13. L-Bracket with longer vertical deformable contact support and more broadly distributed loads.

Table 7
Parameters of the L-Bracket with longer vertical deformable contact support and more broadly distributed loads.

Design Domains	
L	1 mm
$E_{\min}$	1 MPa
$E_{\max}$	210000 MPa
ν	0.3
Contact Supports	
E	420000 MPa
ν	0.3
Distributed Load	
$\boldsymbol{q}$	(0, 2 N)
Stress Limit	
$\sigma_{\lim}$	100 MPa
$\widetilde{\sigma}_{\lim}$	99 MPa

the parameters used for the design domain and the optimization are shown in Table 7. For this setup, convergence problems were observed with the standard augmented Lagrangian approach, both when using linear elastic and hyperelastic material behavior. In particular, the optimizer becomes trapped in infeasible local minima associated with high stresses near the contact surface. Although this behavior is observed for both material models, only the optimized results obtained with the hyperelastic material are presented in the following.

To address this issue, we propose an extended augmented Lagrangian approach (XAL), see Section 3.3.1. The approach extends the standard augmented Lagrangian approach by an additional penalty contribution based on all elements located in the vicinity of the contact surfaces. This extension guides the optimization away from infeasible designs with local stress violations at the contact surfaces. Once the stress constraints at the contact surfaces are satisfied, the additional weighted contribution vanishes, and the formulation reduces to the standard augmented Lagrangian approach.

The optimized designs based on the augmented Lagrangian approach (AL), the extended augmented Lagrangian approach (XAL) and Aggregation with $P_{\max} = 100$ (AGG 100) are shown in Fig. 14 and Table 8 provides additional information on the shown designs. What strikes first is that the optimized design using AL, see Fig. 14(a) fails, as the four elements of the contact surface at the tip of the L-Bracket do not meet the stress constraints at all. A closer look at the convergence history of the maximum stress for the AL method (in blue) shows that it remains

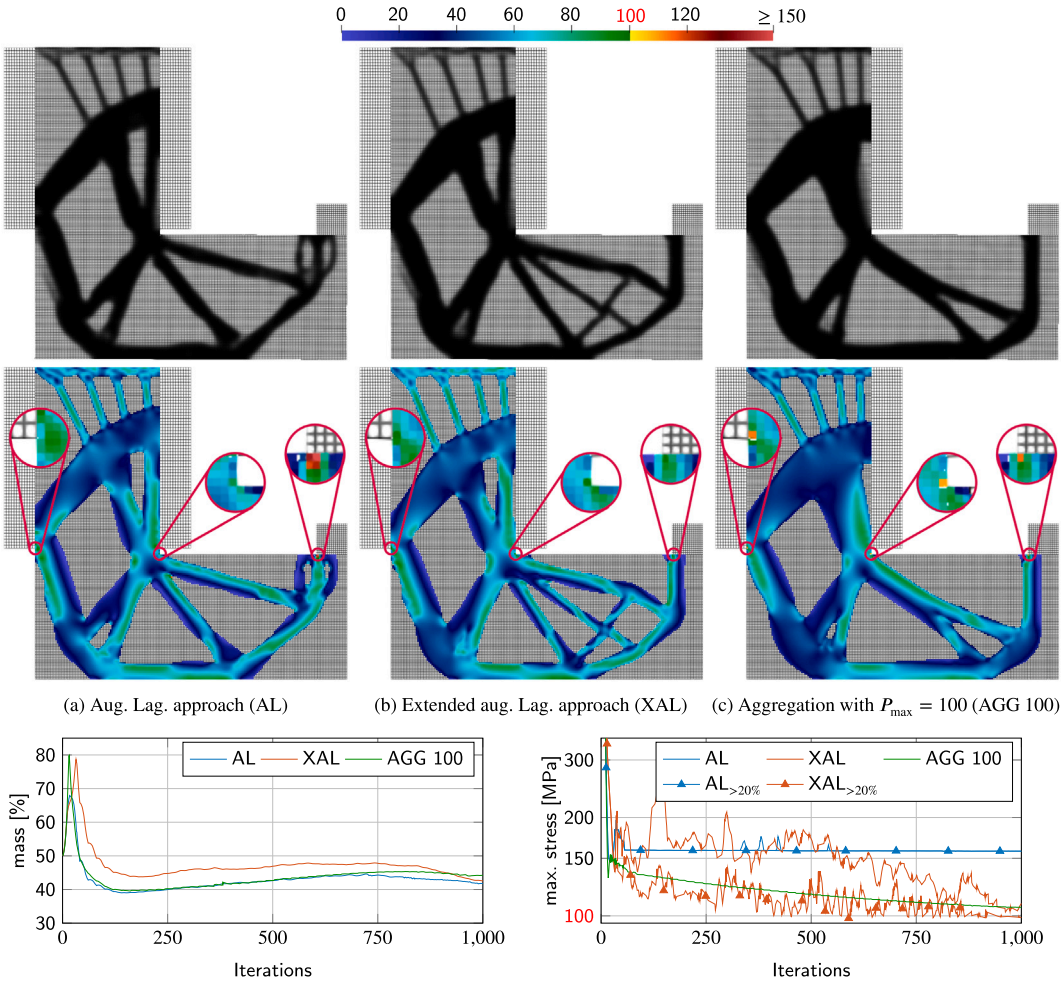

Fig. 14. Optimized designs in deformed configuration and convergence history using the augmented Lagrangian approach (AL), the extended augmented Lagrangian approach (XAL) and aggregation with P_{max} = 100 (AGG 100). All designs are computed using s2s-HSM contact modeling.

Table 8
Details about the designs of Fig. 14 using the standard augmented Lagrangian approach (AL), the extended augmented Lagrangian approach (XAL) and aggregation with P_{max} = 100.

	Iterations	Mass [%]	Max. stress [MPa]	Max. stress with threshold [MPa]
AL	1000	41.7	157.8	157.8
XAL	732	47.7	132.1	99
AGG	1000	44.2	106.2	106.2

around 160 MPa from iteration 20 until the optimization terminates at iteration 1000. Thus, the maximum stress does not improve, while the optimized design's appearance avoids the singularity at the inner edge of the L-Bracket. In fact, the maximum stress value remains in the same two finite elements, which are located at the left end of the horizontal contact surface on the right and have a density between 95% and 100% during the whole optimization. It appears that the optimizer cannot reduce the stresses in these two particular elements and thus does not find a feasible design. In contrast to the former numerical examples, the optimization based on aggregation, see Fig. 14(c), finds a significantly better design, proving that the optimization based on AL is stuck. Nevertheless, AGG 100 also does not fulfill the imposed stress limit, as the stresses in the magnifications are not met. Finally, the proposed extension to the augmented Lagrangian approach overcomes this issue, see Fig. 14(b), where a feasible design is found. This proves that designs exist that satisfy the stress limit.

Different initial guesses for the density distribution and finer discretizations have also been tried. Nevertheless, the standard augmented Lagrangian approach always encounters this problem and is unable to find feasible designs.

It is worth noticing, that the extended augmented Lagrangian approach finds feasible designs for all optimization problems presented in this work. However, the standard augmented Lagrangian approach typically finds slightly lighter designs if it does not become stuck during the optimization process.

5.3. Simultaneous optimization of multiple domains - the U-Bracket indentator

In this Section, a novel benchmark problem for contact- and stress-constrained topology optimization is presented. The problem domain is visualized in Fig. 15(a). The problem contains a U-Bracket which is constrained by Dirichlet conditions at the top edge. The contact surface of the indentation body is defined by its rounded bottom edge. Consequently, the discretized contact surface is blended to the exact geometry using a circular blending function to improve the accuracy of the computed contact pressure. The contact surface of the U-Bracket is planar and therefore does not require blending. The second body is pushed into the U-Bracket by a force q acting on the corner of the top edge. Initially, the contact gap is closed in the center without transmitting a

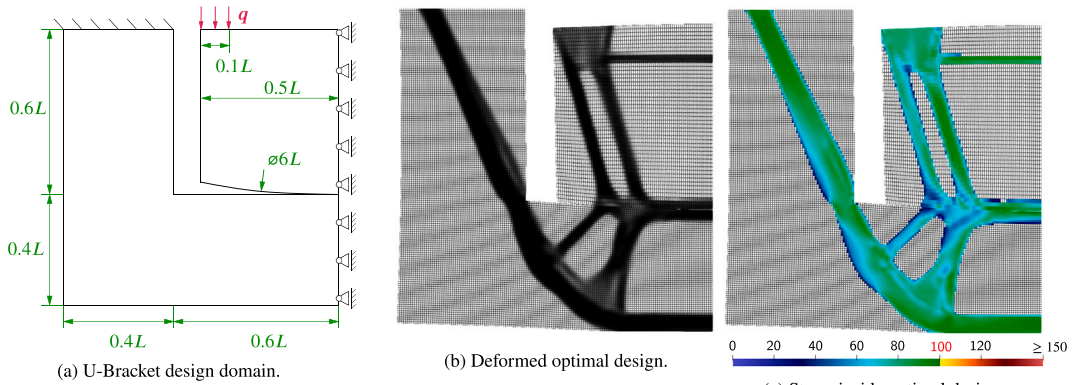

(a) U-Bracket design domain.

(b) Deformed optimal design.

(c) Stress inside optimal design.

Fig. 15. U-Bracket indentation with contact.

Table 9
Parameters of the U-Bracket.

Design Domains	
L	100 mm
$E_{\min}$	1 MPa
$E_{\max}$	5000 MPa
ν	0.3
Distributed load	
$\boldsymbol{q}$	(0, 500 N)
Stress limits	
σ_{lim}	100 MPa
$\tilde{\sigma}_{\text{lim}}$	$0.99 \cdot \sigma_{\text{lim}} = 99$ MPa

contact force. The problem is chosen to have a re-entrant corner similar to the L-Bracket to introduce a singularity to the stress computation. The contact is modeled using the segment-to-segment coupling technique in combination with the HSM constraint.

The objective of the optimization is to minimize the total mass of both contact partners. The optimization is carried out using the standard augmented Lagrangian approach and the parameters are shown in Table 9. In order to demonstrate that other hyperelastic material models can also be used, this example is computed using the compressible Mooney-Rivlin material model.

In doing so, a stress-constrained mass minimization of both contact partners is successfully performed. The optimized design is shown in Fig. 15(b) and the resulting stress field is visualized in Fig. 15(c). It is important to emphasize that the optimized design is relatively stiff and does not exhibit a high amount of large deformations. However, during the early stages of the optimization, the design is dominated by intermediate densities and is much less stiff compared to the optimized design. Therefore, large deformations occur during the first few subproblems until solid struts are formed and the design becomes stiffer. Consequently, hyperelastic material behavior is required to obtain accurate deformations and stresses which are necessary for obtaining accurate gradient information during the early stages of the optimization.

6. Conclusion

This work extends stress-constrained topology optimization to systems involving unilateral contact. The proposed approach is based on hyperelastic material models, enabling the treatment of large deformations. The presented approach minimizes the structure's mass while considering stresses using a local or global stress measure. In doing so, the most common methods for treating stress constraints during the optimization are investigated for a variety of contact problems.

This work demonstrates the influence of node-to-segment and segment-to-segment contact coupling techniques on the optimization. Furthermore, in comparison to more common objectives such as compliance, stress-constrained optimization turns out to be significantly more sensitive to inaccuracies along the contact geometries. Therefore, curved contact surfaces are blended. Thus, the exact geometries of the contact surfaces are considered, as otherwise poorly performing optimized designs are obtained. Using blending functions keeps the computational costs of the optimization process manageable since much finer discretization would otherwise be required to prevent artificial stress peaks near the contact surfaces. Contact constraints are imposed using either a penalty method or a Lagrange methods. The negative effects of an insufficient penalty factor when using a unilateral penalty method for compliance- and stress-constrained topology optimization are demonstrated.

Finally, comparing local and global stress measures for contact problems shows that the augmented Lagrangian approach appears to be better suited, as it has proven to be more reliable in finding feasible designs. An extended augmented Lagrangian approach is proposed, which effectively resolves occasionally occurring convergence issues of the augmented Lagrangian approach. In contrast, the aggregation methods often cannot find feasible designs. Notably, contact-constrained optimizations with high aggregation parameters ($P > 100$) become unstable at lower parameter values than those typically reported in the literature for linear elasticity without contact; see [40]. Overall, the results suggest that a local method to enforce the stress constraints is more appropriate for addressing local mechanical phenomena, such as contact.

Our recommendations for accurate and efficient contact- and stress-constrained mass minimization are:

- The *Hertz-Signorini-Moreau* constraint strictly enforces the contact constraint and is therefore the most accurate, while not requiring any problem-specific tuning.
- Segment-to-segment contact coupling should be preferred over node-to-segment coupling, as it provides smoother contact pressures and stress fields near the contact surfaces.
- Discretizations suitable for compliance optimization may still cause large geometric errors at curved contact surfaces, which can introduce artificial stresses and thereby mislead stress-constrained optimization. These errors can be effectively reduced by blending the discretized contact surfaces onto the exact geometry.
- Stress constraints should be imposed locally using the augmented Lagrangian approach for contact problems as it reliably finds feasible designs with low mass.
- The proposed extended augmented Lagrangian approach should be used for problems where the standard augmented Lagrangian approach becomes trapped in infeasible local minima.

CRediT authorship contribution statement

Timo Schmidt: Writing – review & editing, Writing – original draft, Visualization, Validation, Software, Methodology, Investigation, Conceptualization. **Mirko Keller:** Writing – review & editing, Writing – original draft, Visualization, Validation, Methodology, Investigation, Conceptualization. **Tom Klare:** Writing – review & editing, Methodology, Investigation. **Robert Seifried:** Writing – review & editing, Supervision, Funding acquisition, Conceptualization.

Declaration of competing interest

The authors declare that they have no known competing financial interests or personal relationships that could have appeared to influence the work reported in this paper.

Acknowledgements

This work has been a part of the research training group “Simulation-Based Design Optimization of Dynamic Systems Under Uncertainties” (SENSUS) funded by the state of Hamburg within the Landesforschungsförderung under project number LFF-GK11. Further funding has been provided by Hamburg University of Technology.

Appendix A. Sensitivity analyses

The design update is performed using the Method of Moving Asymptotes [44], so a sensitivity analysis must be performed. The gradient of the objective as well as the gradient of all constraints with respect to the design variables $\boldsymbol{\varphi}$ must be computed. These gradients are efficiently computed using the adjoint method. More precisely, the gradient of the mass as well as the gradient of the used stress criterion are needed, which are derived in the following.

A.1. Gradient of the mass

The gradient of the mass is straightforward; it reads

$$\frac{\partial m(\boldsymbol{\varphi})}{\partial \varphi_i} = \frac{v_i}{v_t}, \tag{65}$$

where v_i is the volume of the considered finite element and v_t is the total volume of the design space.

A.2. Gradient of the element-wise stress constraint

The gradient of the element-wise stress constraint of Eq. (51) is needed for any stress-based topology optimization and is therefore derived separately. In doing so, the chain rule is applied so that the gradient can be written as

$$\frac{\partial g_j}{\partial \varphi_i} = \frac{1}{\sigma_{\text{lim}}} \frac{\partial \sigma_j^{\text{v}}}{\partial \boldsymbol{\sigma}_j} \frac{\partial \boldsymbol{\sigma}_j}{\partial \boldsymbol{x}} \frac{\partial \boldsymbol{x}}{\partial \varphi_i}, \tag{66}$$

where the gradient of the von Mises yield criterion σ_j^{v} with respect to the stress tensor is

$$\frac{\partial \sigma_j^{\text{v}}}{\partial \boldsymbol{\sigma}_j} = \frac{\boldsymbol{V}_0 \boldsymbol{\sigma}_j}{\sigma_j^{\text{v}}}. \tag{67}$$

Next, the derivative of the stress tensor with respect to the state vector $\boldsymbol{x}$ is derived. As mentioned in Section 2.5 the size of the state vector $\boldsymbol{x}$ depends on the used contact constraint formulation, as either a Lagrange method or a unilateral penalty method can be employed to enforce the contact constraints. If the Lagrange method is used, the state vector is $\boldsymbol{x} = \boldsymbol{x}^{\text{LM}} = (\boldsymbol{u}_{\text{S}}, \boldsymbol{u}_{\text{P}}, \boldsymbol{P}_{\text{N}})^{\text{T}}$, whereas otherwise, the unilateral penalty method is used, where the state vector is $\boldsymbol{x} = \boldsymbol{x}^{\text{UP}} = (\boldsymbol{u}_{\text{S}}, \boldsymbol{u}_{\text{P}})^{\text{T}}$. The Lagrange method enforcing the contact constraints must not be confused with the presented augmented Lagrangian approach to enforce the stress constraints of Section 3.3.

However, the stress tensor of any finite element depends only on its nodal displacements. Thus, the derivative of the stress tensor with respect to the contact forces must always vanish so that the gradient of the stress tensor with respect to the state vector is simplified to

$$\frac{\partial \boldsymbol{\sigma}_j}{\partial \boldsymbol{x}} = \left[\frac{\partial \boldsymbol{\sigma}_j}{\partial \boldsymbol{u}} \; \frac{\partial \boldsymbol{\sigma}_j}{\partial \boldsymbol{P}_{\text{N}}} \right] = \left[\frac{\partial \boldsymbol{\sigma}_j}{\partial \boldsymbol{u}} \; \boldsymbol{0} \right], \tag{68}$$

where $\boldsymbol{u}$ is the corresponding displacement field of the considered design domain. Finally, the derivative of the stress tensor with respect to the displacement field is

$$\frac{\partial \boldsymbol{\sigma}_j}{\partial \boldsymbol{u}} = \frac{\partial \left(\frac{1}{J} \boldsymbol{F} \boldsymbol{S} \boldsymbol{F}^{\text{T}} \right)_j}{\partial \boldsymbol{u}}. \tag{69}$$

As the element-wise stress constraint only depends on the displacements of the primary or secondary domain, the derivations of the adjoint problem for the stress-constrained topology optimization problem found in the literature can be applied directly. The only difference from the derivation provided in the literature is that the contact-constrained residual must be used.

Consequently, the next three sections will provide the necessary literature as well as the resulting adjoint equation and the gradients for the augmented Lagrangian approach and for the P-mean aggregation, respectively.

A.3. Gradient using the augmented Lagrangian approach

The gradient of the penalty term $P^{(k)}$ of the optimization problem from Eq. (53) is outlined in the following, while a detailed derivation can be found in [37]. In doing so, only gradients of active stress constraints must be computed as the gradient of the equality constraint h_j is

$$\frac{\partial h_j(\boldsymbol{\varphi})}{\partial \varphi_i} = \begin{cases} \dfrac{\partial \theta_j(\boldsymbol{\varphi})}{\partial \varphi_i} & \text{, if } \theta_j(\boldsymbol{\varphi}) > -\dfrac{\lambda_j^{(k)}}{\mu^{(k)}} \\ 0 & \text{, else} \end{cases} \tag{70}$$

where θ_j is the vanishing constraint of Eq. (52).

Thus, the gradient of the penalty term is

$$\frac{\partial \boldsymbol{P}^{(k)}(\boldsymbol{\varphi})}{\partial \varphi_i} = \sum_{j=1}^{n_{\text{el}}} \alpha_j w_j \left[\lambda_j^{(k)} + \mu^{(k)} h_j(\boldsymbol{\varphi}) \right] \left(\frac{\partial \theta_j(\boldsymbol{\varphi})}{\partial g_j} \frac{\partial g_j}{\partial \varphi_i} + \delta_i^j \frac{p}{\varphi_i} \theta_i(\boldsymbol{\varphi}) \right), \tag{71}$$

where the parameter $\alpha_j \in \{0, 1\}$ is zero whenever the j-th constraint is inactive and equal to one otherwise. Further, the gradient $\dfrac{\partial g_j}{\partial \varphi_i}$ is known from Eq. (66) and δ_i^j is a Kronecker delta. The gradient of g_j depends on the state vector $\boldsymbol{x}$ so that an adjoint equation is needed to eliminate the costly derivative $\dfrac{\partial \boldsymbol{x}}{\partial \varphi_i}$ which is hidden in Eq. (66). The resulting adjoint equation is

$$\frac{1}{n_{\text{el}}} \sum_{j=1}^{n_{\text{el}}} \alpha_j w_j \left[\lambda_j^{(k)} + \mu^{(k)} h_j(\boldsymbol{\varphi}) \right] \frac{\partial \theta_j(\boldsymbol{\varphi})}{\partial g_j} \frac{1}{\sigma_{\text{lim}}} \frac{\partial \sigma_j^{\text{v}}}{\partial \boldsymbol{\sigma}_j} \frac{\partial \boldsymbol{\sigma}_j}{\partial \boldsymbol{x}} - \boldsymbol{\gamma}^{\text{T}} \boldsymbol{J}_{\text{c}} = \boldsymbol{0}, \tag{72}$$

where the adjoint vector $\boldsymbol{\gamma}$ is introduced and the matrix $\boldsymbol{J}_{\text{c}}$ is the contact Jacobian of Section 2.5. Finally, the gradient of the objective using the standard augmented Lagrangian approach is

$$\frac{\partial \mathcal{L}^{(k)}(\boldsymbol{\varphi})}{\partial \varphi_i} = \frac{v_i}{v_t} + \frac{1}{n_{\text{el}}} \alpha_i w_i \left[\lambda_i^{(k)} + \mu^{(k)} h_i(\boldsymbol{\varphi}) \right] \frac{p}{\varphi_i} \theta_i(\boldsymbol{\varphi}) - \boldsymbol{\gamma}^{\text{T}} \frac{\partial \boldsymbol{J}_{\text{c}}}{\partial \varphi_i} \boldsymbol{x}. \tag{73}$$

A.4. Gradient using the P-mean aggregation function

If the P-mean function is used, the gradient of the stress constraint $\Psi \leq 0$ is obtained using an arbitrary adjoint vector $\hat{\boldsymbol{\gamma}}$ and the contact residual $\boldsymbol{r}_{\mathrm{c}}(\boldsymbol{\varphi}, \hat{\boldsymbol{x}}) = \boldsymbol{0}$ of the solution to the contact problem $\hat{\boldsymbol{x}}$. Thus, the gradient is

$$\frac{\partial \Psi}{\partial \varphi_i} = \frac{\partial}{\partial \varphi_i}\left[\left(\frac{1}{n_{\mathrm{el}}}\sum_{j=1}^{n_{\mathrm{el}}}(\Theta_j+1)^P\right)^{(1/P)} - 1\right] - \hat{\boldsymbol{\gamma}}^{\mathrm{T}}\frac{\partial \boldsymbol{r}_{\mathrm{c}}(\boldsymbol{\varphi}, \hat{\boldsymbol{x}})}{\partial \varphi_i} \tag{74}$$

In doing so, the adjoint equation is

$$\boldsymbol{0} = \frac{1}{n_{\mathrm{el}}}\left(\frac{1}{n_{\mathrm{el}}}\sum_{k=1}^{n_{\mathrm{el}}}(\Theta_k+1)^P\right)^{(1/P)-1}\sum_{j=1}^{n_{\mathrm{el}}}(\Theta_j+1)^{(P-1)}\frac{1}{\sigma_{\mathrm{lim}}}\frac{\partial \sigma_j^{\mathrm{v}}}{\partial \boldsymbol{\sigma}_j}\frac{\partial \boldsymbol{\sigma}_j}{\partial \boldsymbol{x}} - \hat{\boldsymbol{\gamma}}^{\mathrm{T}}\boldsymbol{J}_{\mathrm{c}} \tag{75}$$

and the resulting gradient using the adjoint vector $\hat{\boldsymbol{\gamma}}$ solving Eq. (75) is

$$\frac{\partial \Psi}{\partial \varphi_i} = \frac{1}{n_{\mathrm{el}}}\left(\frac{1}{n_{\mathrm{el}}}\sum_{k=1}^{n_{\mathrm{el}}}(\Theta_k+1)^P\right)^{(1/P)-1}\sum_{j=1}^{n_{\mathrm{el}}}(\Theta_j+1)^{(P-1)}\delta_i^j g_i - \hat{\boldsymbol{\gamma}}^{\mathrm{T}}\frac{\partial \boldsymbol{J}_{\mathrm{c}}}{\partial \varphi_i}\hat{\boldsymbol{x}}. \tag{76}$$

Appendix B. The influence of blending in compliance optimization

In the following, the compliance optimizations of the modified benchmark example of [43] are shown. All optimizations are terminated after 100 iterations and the volume constraint allows filling up to 30% of the total volume of the design domain. In doing so, both contact partners are deformable, and the parameters are unchanged from the ones used for the stress-constrained topology optimization of Section 5.1.

The optimized designs of Figs. 16 and 17 show that modeling the contact surfaces accurately using a circular blending function is not necessary if the contact support is deformable and the compliance is minimized. This can be observed, as the optimized designs obtained with and without blending are very similar, even though the computed contact pressures are dominated by artificial contact pressure peaks, see Fig. 8. This observation holds true for node-to-segment and segment-to-segment contact coupling. As shown in both figures, the compliance-optimized designs a and d, b and e or c and f are more or less identical. This is a major difference from stress-constrained topology optimization, where accurately modeling the contact surface is crucial to obtain physically meaningful optimized designs. However, a penalty factor that is too small has a significant influence on the optimized designs, so a sufficiently high penalty value ϵ must be chosen.

Appendix C. The influence of blending in mass minimization

In this Section, the mass minimization problem of Section 5.1 is considered and results with and without the circular blending function are shown. In doing so, only the HSM contact constraint is used. However, the results are directly transferable to optimizations based on the unilateral penalty (UP) contact constraint. If UP is used, the penalty factor must of course be sufficiently high, as discussed in this work. Additionally, the optimized results of this Section are based on the augmented Lagrangian approach and two discretizations of the the inner contact structure are used. The results of the optimizations are shown in Fig. 18 and further details for each optimized design is provided in Table 10. The Fig. 18(a) and (d) use the same discretization as the one used in Section 5.1 so that these designs can be directly compared to the optimized design with blending of Fig. 9. The other four optimized designs are computed based on a coarser inner contact structure consisting of 273 triangular finite elements, whereas the default discretization consists of 1206 quadrilateral finite elements. The designs of Fig. 18(b) and (e) are computed without blending, while Fig. 18(c) and (f) use a circular blending function to show the influence of blending for the coarse discretization of the contact surfaces. In doing so, all design that do not use the circular blending function, have gray to void elements at the contact surface. These empty elements occur, because the optimization tries to avoid discretization dependent stress peaks at the contact

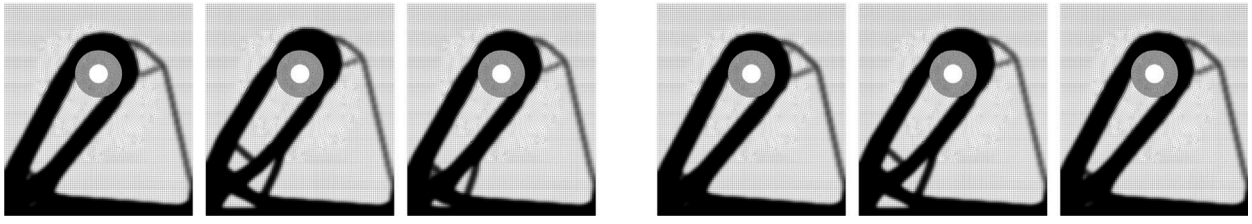

(a) n2s-HSM. (b) n2s-UP1. (c) n2s-UP2. (d) bl. n2s-HSM. (e) bl. n2s-UP1. (f) bl. n2s-UP2.

Fig. 16. Compliance optimization for node-to-segment coupling and a deformable contact support. Exact modeling of the contact surface using a circular blending function is labeled as 'bl.'.

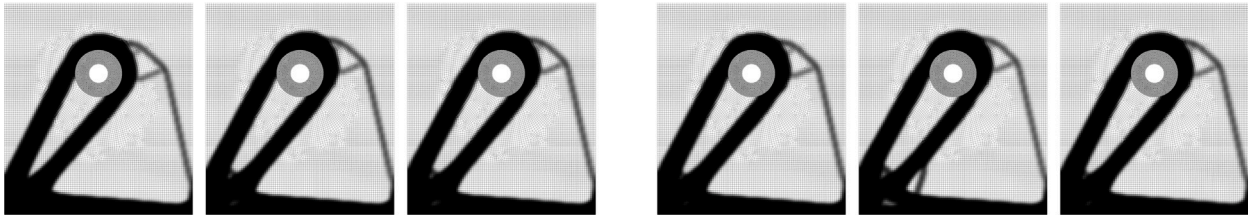

(a) s2s-HSM. (b) s2s-UP1. (c) s2s-UP2. (d) bl. s2s-HSM. (e) bl. s2s-UP1. (f) bl. s2s-UP2.

Fig. 17. Compliance optimizations for segment-to-segment coupling and a deformable contact support. Exact modeling of the contact surface using a circular blending function is labeled as 'bl.'.

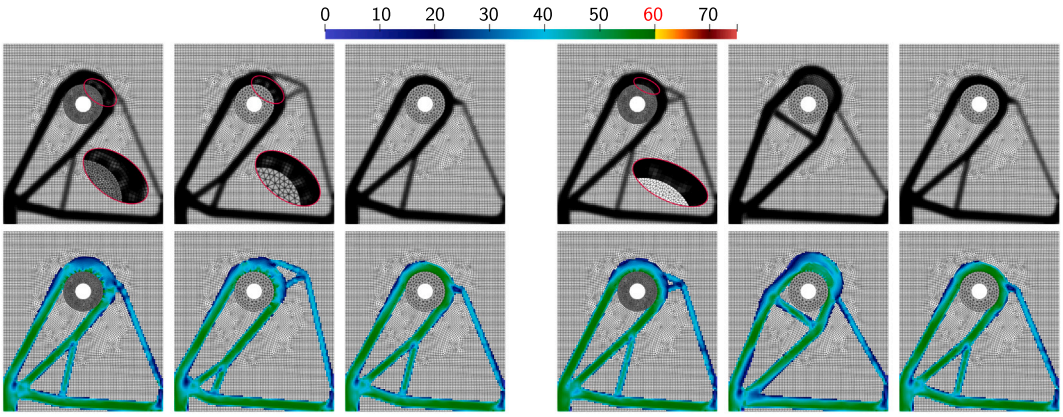

(a) n2s-HSM not blended (b) n2s-HSM not blended with coarser inner contact support (c) n2s-HSM blended with coarser inner contact support (d) s2s-HSM not blended (e) s2s-HSM not blended with coarser inner contact support (f) s2s-HSM blended with coarser inner contact support

Fig. 18. Best designs using the augmented Lagrangian approach without and with blending. Two different discretizations of the inner disc-like contact domain are used.

Table 10
Details about the designs of Fig. 18 obtained using the augmented Lagrangian approach.

	Coupling	Iterations	Mass [%]	Max. stress [MPa]
no blending	n2s s2s	1009 1026	20.1 19.2	59.5 60.0
coarse no blending	n2s s2s	1092 1056	19.9 22.3	59.5 60.0
coarse with blending	n2s s2s	1073 996	18.8 18.8	59.5 60.0

surface. This is nonphysical behavior and results in poor performing designs in practice. If the optimized designs – obtained without blending – are reevaluated with a the circular blending function, the stress limit is not met. Thus, the contact geometry must be modeled accurately, as otherwise the optimization will end up in a poorly performing optimized design.

Data availability

Data will be made available upon request.

References

[1] Andrade-Campos A, Ramos A, Simões JA. A model of bone adaptation as a topology optimization process with contact. J Biomed Sci Eng 2012;5:229–44.
[2] Balay S, Abhyankar S, Adams MF, Benson S, Brown J, Brune P, Buschelman K, Constantinescu E, Dalcin L, Dener A, Eijkhout V, Faibussowitsch J, Gropp WD, Hapla V, Isaac T, Jolivet P, Karpeev D, Kaushik D, Knepley MG, Kong F, Kruger S, May DA, McInnes LC, Mills RT, Mitchell L, Munson T, Roman JE, Rupp K, Sanan P, Sarich J, Smith BF, Zampini S, Zhang H, Zhang H, Zhang J. PETSc/TAO users manual. Technical Report ANL-21/39 - Revision 3.21 Argonne National Laboratory; 2024.
[3] Balay S, Abhyankar S, Adams MF, Benson S, Brown J, Brune P, Buschelman K, Constantinescu EM, Dalcin L, Dener A, Eijkhout V, Faibussowitsch J, Gropp WD, Hapla V, Isaac T, Jolivet P, Karpeev D, Kaushik D, Knepley MG, Kong F, Kruger S, May DA, McInnes LC, Mills RT, Mitchell L, Munson T, Roman JE, Rupp K, Sanan P, Sarich J, Smith BF, Zampini S, Zhang H, Zhang H, Zhang J. PETSc web page; 2024. https://petsc.org/.
[4] Balay S, Gropp WD, McInnes LC, Smith BF. Efficient management of parallelism in object oriented numerical software libraries. In: Arge E, Bruaset AM, Langtangen HP, editors. Modern software tools in scientific computing. Birkhäuser Press; 1997. p. 163–202.
[5] Bathe K-J, Chaudhary A. A solution method for planar and axisymmetric contact problems. Int J Numer Methods Eng 1985;21:65–88.
[6] Bendsøe MP, Sigmund O. Topology optimization: theory, methods and applications. 2 ed. Berlin, Heidelberg: Springer Science and Business Media; 2013.
[7] Boyd SP, Vandenberghe L. Convex optimization. Cambridge and New York, NY and Port Melbourne: Cambridge University Press; 2004.
[8] Bruggi M. On an alternative approach to stress constraints relaxation in topology optimization. Struct Multidiscip Optim 2008;36(2):125–41.
[9] Bruggi M, Duysinx P. A stress–based approach to the optimal design of structures with unilateral behavior of material or supports. Struct Multidiscip Optim Aug 2013;48(2):311–26.
[10] Chen X, Hisada T. Development of a finite element contact analysis algorithm to pass the patch test. JSME Int J Solid Mech Mater Eng 4 2006;49:483–91.
[11] Chen Y, Monteiro E, Koutiri I, Favier V. Stress-constrained topology optimization using the constrained natural element method. Struct Multidiscip Optim 2024;67(4):65.
[12] Cheng GD, Guo X. ε-relaxed approach in structural topology optimization. Struct Multidiscip Optim 1997;13(4):258–66.
[13] Silva GAD, Aage N, Teófilo Beck A, Sigmund O. Three–dimensional manufacturing tolerant topology optimization with hundreds of millions of local stress constraints. Int J Numer Methods Eng 2021;122(2):548–78.
[14] Duysinx P, Bendsøe MP. Topology optimization of continuum structures with local stress constraints. Int J Numer Methods Eng 1998;43(8):1453–78.
[15] Fancello EA. Topology optimization for minimum mass design considering local failure constraints and contact boundary conditions. Struct Multidiscip Optim 2006;32(3):229–40.
[16] Fernandez F, Puso MA, Solberg J, Tortorelli DA. Topology optimization of multiple deformable bodies in contact with large deformations. Comput Methods Appl Mech Eng 11 2020;371:113288.
[17] Gordon WJ, Hall CA. Transfinite element methods: blending-function interpolation over arbitrary curved element domains. Numer Math 1973;21:109–29.
[18] Hallquist JO, Goudreau GL, Benson DJ. Sliding interfaces with contact-impact in large-scale Lagrangian computations. Comput Methods Appl Mech Eng 9 1985;51:107–37.
[19] Hallquist JO. Nike2d: an implicit, finite-deformation, finite-element code for analyzing the static and dynamic response of two-dimensional solids. Technical report Livermore (USA). Lawrence Livermore Lab: California Univ.; 1979.
[20] Han Y, Bin X, Duan Z, Huang X. Stress-based topology optimization of continuum structures for the elastic contact problems with friction. Struct Multidiscip Optim Feb 2022;65(2):54.
[21] Holmberg E, Torstenfelt B, Klarbring A. Stress constrained topology optimization. Struct Multidiscip Optim 7 2013;48:33–47.
[22] Xueyan H, Zonghao L, Bao R, Chen W, Wang H. An adaptive method of moving asymptotes for topology optimization based on the trust region. Comput Methods Appl Mech Eng 2022;393(114202).
[23] Hughes TJR, Taylor RL, Kanoknukulchai W. A finite element method for large displacement contact and impact problems. In: Bathe KJ, Oden JT, Wunderlich W, editors. Formulations and computational algorithms in finite element analysis. Cambridge, MA: The MIT Press; 1977. p. 468–95.
[24] Hughes TJR, Taylor RL, Sackman JL, Curnier A, Kanoknukulchai W. A finite element method for a class of contact-impact problems. Comput Methods Appl Mech Eng 7 1976;8:249–76.
[25] James KA, Lee E, Martins JRRA. Stress-based topology optimization using an isoparametric level set method. Finite Elem Anal Des 2012;58:20–30.
[26] Klarbring A, Strömberg N. Topology optimization of hyperelastic bodies including non-zero prescribed displacements. Struct Multidiscip Optim 2013;47(1):37–48.
[27] Chau L, Norato J, Bruns T, Christopher H, Tortorelli D. Stress-based topology optimization for continua. Struct Multidiscip Optim 4 2010;41:605–20.
[28] Luo Y, Ming L, Kang Z. Topology optimization of hyperelastic structures with frictionless contact supports. Int J Solids Struct 3 2016;81:373–82.
[29] Mankame ND, Ananthasuresh GK. Topology optimization for synthesis of contact-aided compliant mechanisms using regularized contact modeling. Comput Struct 2004;82(15–16):1267–90.

[30] Moreau JJ. On unilateral constraints. In: Friction and plasticity, vol. 63. Springer, Berlin, Heidelberg; 2011. p. 171–322.
[31] Papadopoulos P, Taylor RL. A mixed formulation for the finite element solution of contact problems. Comput Methods Appl Mech Eng 2 1992;94:373–89.
[32] Popp A, Gitterle M, Gee MW, Wall WA. A dual mortar approach for 3D finite deformation contact with consistent linearization. Int J Numer Methods Eng 9 2010;83:1428–65.
[33] Puso MA, Laursen TA. A mortar segment-to-segment contact method for large deformation solid mechanics. Comput Methods Appl Mech Eng 2 2004;193:601–29.
[34] Puso MA, Laursen TA. A mortar segment-to-segment frictional contact method for large deformations. Comput Methods Appl Mech Eng 11 2004;193:4891–913.
[35] Rinderer L, Popp A, Gee MW. Topology optimization of 3D finite deformation frictional mortar contact problems using adjoint sensitivities. Comput Methods Appl Mech Eng 2026;449(118507).
[36] Schmidt T, Kriegesmann B, Seifried R. Robust contact-constrained topology optimization considering uncertainty at the contact support. Struct Multidiscip Optim 4 2024;67:1–15.
[37] Senhora FV, Giraldo-Londoño O, Menezes IFM, Paulino GH. Topology optimization with local stress constraints: a stress aggregation-free approach. Struct Multidiscip Optim 2020;62(4):1639–68.
[38] Sigmund O. Morphology-based black and white filters for topology optimization. Struct Multidiscip Optim 2007;33:401–24.
[39] Signorini A. Questioni DI elasticità non linearizzata e semilinearizzata. Rend Mat Appl 1959;5:95–139.
[40] da Silva GA, Aage N, Beck AT, Sigmund O. Local versus global stress constraint strategies in topology optimization: a comparative study. Int J Numer Methods Eng 2021;122:6003–36.
[41] Simo JC, Wriggers P, Taylor RL. A perturbed Lagrangian formulation for the finite element solution of contact problems. Comput Methods Appl Mech Eng 8 1985;50:163–80.
[42] Strömberg N. Topology optimization of orthotropic elastic design domains with mortar contact conditions. In: World congress of structural and multidisciplinary optimisation. Springer; 2017. p. 1427–38.
[43] Strömberg N, Klarbring A. Topology optimization of structures in unilateral contact. Struct Multidiscip Optim 2010;41:57–64.
[44] Svanberg K. The method of moving asymptotes - a new method for structural optimizaion. Int J Numer Methods Eng 1987;24:359–73.
[45] Sved G, Ginos Z. Structural optimization under multiple loading. Int J Mech Sci 1968;10(10):803–5.
[46] Taylor RL, Papadopoulos P. On a patch test for contact problems in two dimensions. Comput Methods Nonlinear Mech 1991;690(702).
[47] Verbart A, Langelaar M, van Keulen F, MLangelaar ML, van Keulen AvanKeulen TF. A unified aggregation and relaxation approach for stress-constrained topology optimization. Struct Multidiscip Optim 2017;55:663–79.
[48] Wang F, Lazarov BS, Sigmund O. On projection methods, convergence and robust formulations in topology optimization. Struct Multidiscip Optim 2011;43(6):767–84.
[49] Wilking C, Bischoff M. Alternative integration algorithms for three-dimensional mortar contact. Comput Mech 2 2017;59:203–18.
[50] Wriggers P. A note on tangent stiffness for fully nonlinear contact problems. Commun Appl Numer Methods 1985;1:199–203.
[51] Wriggers P, Van TV, Stein E. Finite element formulation of large deformation impact-contact problems with friction. Comput Struct 1990;37:319–31.
[52] Wriggers P. Computational contact mechanics. Berlin Heidelberg, Berlin, Heidelberg: Springer; 2006.
[53] Zavarise G, De Lorenzis L. The node-to-segment algorithm for 2D frictionless contact: classical formulation and special cases. Comput Methods Appl Mech Eng 2009;198(41):3428–51.
[54] Zavarise G, De Lorenzis L. A modified node-to-segment algorithm passing the contact patch test. Int J Numer Methods Eng 7 2009;79:379–416.
[55] Zhai X, Chen F, Jun W. Alternating optimization of design and stress for stress-constrained topology optimization. Struct Multidiscip Optim Oct 2021;64(4):2323–42.
[56] Zienkiewicz OC, Taylor RL, Zhu JZ. The finite element method: its basis & fundamentals. 7th ed. Elsevier: Butterworth-Heinemann; 2014.
[57] Zienkiewicz OC, Taylor RL, Zhu JZ. Chapter 6 - shape functions, derivatives, and integration. In: Zienkiewicz OC, Taylor RL, Zhu JZ, editors. The finite element method: its Basis and fundamentals, 7th ed. Butterworth-Heinemann, Oxford; 2013. p. 151–209.